Government of Western Australia

Department of
Mines and Petroleum

REPORT
121

A MAGNETOTELLURIC TRAVERSE ACROSS THE SOUTHERN YILGARN CRATON

by MC Dentith, S Evans, S Thiel, L Gallardo, A Joly, and SS Romano

ROYALTIES FOR REGIONS
EXPLORATION INCENTIVE SCHEME

Centre for EXPLORATION TARGETING

Geological Survey of Western Australia

Government of Western Australia
Department of Mines and Petroleum

REPORT 121

A MAGNETOTELLURIC TRAVERSE ACROSS THE SOUTHERN YILGARN CRATON

by
MC Dentith[1], S Evans[2], S Thiel[3], L Gallardo[1], A Joly[1], and SS Romano

[1] Centre for Exploration Targeting, The University of Western Australia, 35 Stirling Highway, Crawley, Perth WA 6009

[2] Moombarriga Geoscience, 32 Townshend Road, Subiaco WA 6008

[3] TRaX, Mawson Building, North Terrace Campus, The University of Adelaide, Adelaide SA 5005

Perth 2013

Geological Survey of
Western Australia

MINISTER FOR MINES AND PETROLEUM
Hon. Bill Marmion MLA

DIRECTOR GENERAL, DEPARTMENT OF MINES AND PETROLEUM
Richard Sellers

EXECUTIVE DIRECTOR, GEOLOGICAL SURVEY OF WESTERN AUSTRALIA
Rick Rogerson

REFERENCE
The recommended reference for this publication is:
Dentith, M, Evans, S, Thiel, S, Gallardo, L, Joly, A and Romano, SS 2013, A magnetotelluric traverse across the southern Yilgarn Craton: Geological Survey of Western Australia, Report 121, 43p.

National Library of Australia Cataloguing-in-Publication entry

Author: Dentith, Mike, author.

Title: A magnetotelluric traverse across the southern Yilgarn Craton / Michael Dentith ; Shane Evans ; Stephan Thiel; Luis Gallardo ; Aurore Joly ; Sandra S. Romano.

ISBN: 9781741684896 (electronic document)

Series: Report (Geological Survey of Western Australia) ; 121.

Subjects: Magnetotelluric methods--Western Australia--Yilgarn Block.

Other Authors/Contributors: Evans, Shane, author.
Thiel, Stephan, author.
Gallardo, Luis, author.
Joly, Aurore, author.
Romano, Sandra S., author.

Dewey Number: 622.153

ISSN 0508–4741

Grid references in this publication refer to the Geocentric Datum of Australia 1994 (GDA94). Locations mentioned in the text are referenced using Map Grid Australia (MGA) coordinates, Zone 51. All locations are quoted to at least the nearest 100 m.

Copy editor: A Forbes
Cartography: M Prause
Desktop publishing: RL Hitchings
Printed by Images on Paper, Perth, Western Australia

Published 2013 by Geological Survey of Western Australia
This Report is published in digital format (PDF) and is available online at <www.dmp.wa.gov.au/GSWApublications>.

Further details of geological publications and maps produced by the Geological Survey of Western Australia are available from:
Information Centre
Department of Mines and Petroleum
100 Plain Street
EAST PERTH WESTERN AUSTRALIA 6004
Telephone: +61 8 9222 3459 Facsimile: +61 8 9222 3444
www.dmp.wa.gov.au/GSWApublications

Cover image: Laying out an electrode during acquisition of the southern Yilgarn Craton magnetotelluric traverse.

Contents

Appendix

Figures

Tables

A magnetotelluric traverse across the southern Yilgarn Craton

by

MC Dentith[1], S Evans[2], S Thiel[3], L Gallardo[1], A Joly[1], and SS Romano

Abstract

A 300-km-long magnetotelluric survey, comprising 56 stations, has been completed in the southern Yilgarn Craton over three campaigns during 2009–11. The survey was conducted along an east–west traverse extending from the South West Terrane, across the Southern Cross Domain (Youanmi Terrane), and onto the Kalgoorlie Terrane (Eastern Goldfields Superterrane).

The magnetotelluric data were processed with robust remote-reference algorithms. Data shown by phase-tensor analysis to represent 1D and 2D variations in electrical properties were modelled using industry-standard inverse modelling methods. A geoelectric strike direction of 010° was used for the modelling. Electrical conductivity variations to depths greater than 100 km have been mapped and interpreted.

The preferred resistivity cross section shows a series of narrow, dipping zones of increased conductivity in the crustal part of the model. These are interpreted as major faults that, in some areas, correlate with known surface structures. Resistivity variations at lower crust and mantle depths show that the local lithosphere comprises three recognisable units with probably steep boundaries. The three-fold subdivision of the local lithosphere is consistent with the geologically and geochemically defined terranes and domains in this part of the Yilgarn Craton. The central unit, interpreted as equivalent to the Southern Cross Domain, has a resistive crust overlying a more conductive mantle. The unit to the east comprises a conductive lower crust overlying a resistive mantle. The eastern margin of the Southern Cross Domain, as inferred from deep crustal and mantle resistivity, lies about 50 km to the west of the Ida Fault, the margin of the domain at the surface. The disparity with the mapped location of the Ida Fault may reflect incorrect mapping of the Ida Fault, or offset of near-surface and deep-crustal and mantle suture zones, or both. The western margin of the central unit is interpreted to coincide with the western edge of a zone of more conductive mantle. The western unit has a resistive crust overlying a resistive mantle and is correlated with the South West Terrane mapped at the surface. Several conductive features in the crust might be linked to the edge of the zone of conductive mantle, but surface geology suggests the boundary is comparatively steep and coincides with a conductive zone close to the western edge of the Southern Cross greenstone belt.

The magnetotelluric method has been demonstrated to be a viable means of mapping the deep-crustal and mantle structure of the Yilgarn Craton.

KEYWORDS: magnetotelluric surveys, electrical resistivity, geophysical models, Bouguer anomaly maps, TMI maps, structural terranes, South West Terrane, Youanmi Terrane, Eastern Goldfields Superterrane, Yilgarn Craton, Western Australia

[1] Centre for Exploration Targeting, The University of Western Australia, 35 Stirling Highway, Crawley, Perth WA 6009

[2] Moombarriga Geoscience, 32 Townshend Road, Subiaco WA 6008

[3] TRaX, Mawson Building, North Terrace Campus, The University of Adelaide, Adelaide SA 5005

Introduction

A magnetotelluric (MT) traverse funded by the Western Australian Government's Exploration Incentive Scheme has been completed across the southern Yilgarn Craton from near Hyden to near Norseman (Figs 1 and 2). The survey comprises an approximately east–west traverse that crosses the boundaries between the South West Terrane, Youanmi Terrane (Southern Cross Domain), and Kalgoorlie Terrane (Eastern Goldfields Superterrane).

The MT method is a deep-penetrating, passive (natural-source), usually frequency-domain electromagnetic method that allows variations in electrical conductivity in the crust and upper mantle to be mapped. A comprehensive description of the method is given by Simpson and Bahr (2005). Briefly, natural fluctuating magnetic fields due to the interaction of the geomagnetic field with solar winds and, at higher frequencies, lightning strikes, induce telluric (electric) currents in the Earth. These variations span a broad range of frequencies. Note that the terms frequency and period are used interchangeably when describing MT data. Frequency (f) in hertz (Hz) is the reciprocal of period (P) in seconds (s).

It is because magnetic fields vary at a range of frequencies that electrical conductivity variations at depth can be determined. The penetration (i.e. attenuation with distance) of an electromagnetic field into a medium depends on the medium's electrical conductivity and the frequency of the variations in the electromagnetic field. Lower frequencies penetrate more deeply and greater subsurface conductivity reduces penetration for a given frequency. After recording, the electric and magnetic fields can be mathematically separated into components with different frequencies, and therefore electrical properties at different depths can be estimated. For this reason, in the descriptions in this Report of the processing and interpretation of the MT data, period can be thought of as a proxy for depth. However, because the conductivity of the Earth varies from location to location, the conversion factor from period to depth also varies. The maximum period (depth) of interest dictates the length of the time interval over which the variations in the electric and magnetic fields must be recorded. To achieve penetration to mantle depths requires recording for some tens of hours.

For much of its extent, the MT survey followed the Hyden–Norseman road, making access straightforward, although, to avoid the effects of traffic, stations were located at least 150 m from the road. East of the Koolyanobbing Shear Zone (Fig. 2), the current road coincides with a major Proterozoic dyke, the Jimberlana dyke. It was uncertain whether the dyke was electrically distinct from the country rock, perhaps due to its conductive sulfide content (Mazzucchelli and Robins, 1973). To avoid the possibility of sampling atypical crust, east of Lake Johnston the survey followed the old Hyden–Norseman road, about 20 km north of the dyke. This road is no longer maintained, but is accessible using 4WD vehicles. Following the old road meant that the MT traverse was not linear; however, this disadvantage was considered acceptable to avoid the possibility of the Jimberlana dyke affecting the data. It was subsequently demonstrated that the dyke did not affect MT responses.

The MT traverse links areas with significantly different geochemical characteristics, and passes through areas that contain significant mineral deposits, notably nickel–sulfide deposits in greenstone belt rocks. The traverse crosses three greenstone belts: the Southern Cross – Forrestania greenstone belt, the Lake Johnston greenstone belt, and the Norseman–Wiluna greenstone belt. Greenstone rocks in the Southern Cross – Forrestania and Lake Johnston belts are typically older than those in the Norseman–Wiluna belt; ages are up to 2.9 Ga (Wang et al., 1996; Mueller and McNaughton, 2000). Rocks in the Norseman area have been dated at 2.7 Ga, although there is evidence of local older components (Pidgeon and Wilde, 1990). Moreover, a Nd-isotope study of granites of the Yilgarn Craton (Cassidy and Champion, 2004) showed significant differences in granites of the Eastern Goldfields Superterrane compared to those of other terranes crossed by the MT traverse. Multi-isotopic whole-rock analyses of zircons from intrusive and volcanic rocks have revealed how the lithosphere has evolved through time in the Yilgarn Craton (Mole et al., 2010). These data imply the presence of a paleocratonic boundary in the survey area and it has been argued that such features are linked to the occurrence of magmatic nickel–sulfide and gold deposits see for example, Begg et al. (2010).

The location of the implied suture zone between the geologically and geochemically different areas is poorly defined, and it is uncertain whether known large-scale structures correspond to the suture or if there are major structures yet to be identified. Moreover, the position and geometry at depth of the known major structures in the study area is unknown or poorly constrained; for example, the Ida Fault (Figs 1 and 2). An improved understanding of the extent and relationships of major crustal domains and terranes with the intervening large-scale structures in the study area was the primary motivation for the MT survey. The interpretation reported here emphasises crustal and upper mantle responses.

Regional geology

The Archean Yilgarn Craton consists of 3000–2620 Ma, poly-deformed, northerly trending greenstone belts separated by granite and granitic gneiss (Gee, 1981; Pidgeon and Wilde, 1990; Wang et al., 1996; Schiøtte and Campbell, 1996; Pidgeon and Hallberg, 2000; Kositcin et al., 2008; Van Kranendonk and Ivanic, 2009). The period 2800–2600 Ma was one of the major periods of growth of continental crust recorded in granite–greenstone terrains (Condie, 1997) that also formed world-class metallogenic provinces (Barley and Groves, 1987; Groves and Barley, 1994; Barley et al., 1998; McCuaig and Kerrich, 1998; Hoatson et al., 2011).

The Yilgarn Craton has been divided into seven terranes that are bounded by major shear zones and fault systems (Fig. 1; Cassidy et al., 2006; Pawley et al., 2009). Greenstones in the Youanmi Terrane are metamorphosed to greenschist or amphibolite facies (Ahmat, 1986; Goscombe et al., 2009), whereas the South West Terrane contains granulite facies supracrustal rocks (Qiu and Groves, 1999). Both regions contain voluminous granites.

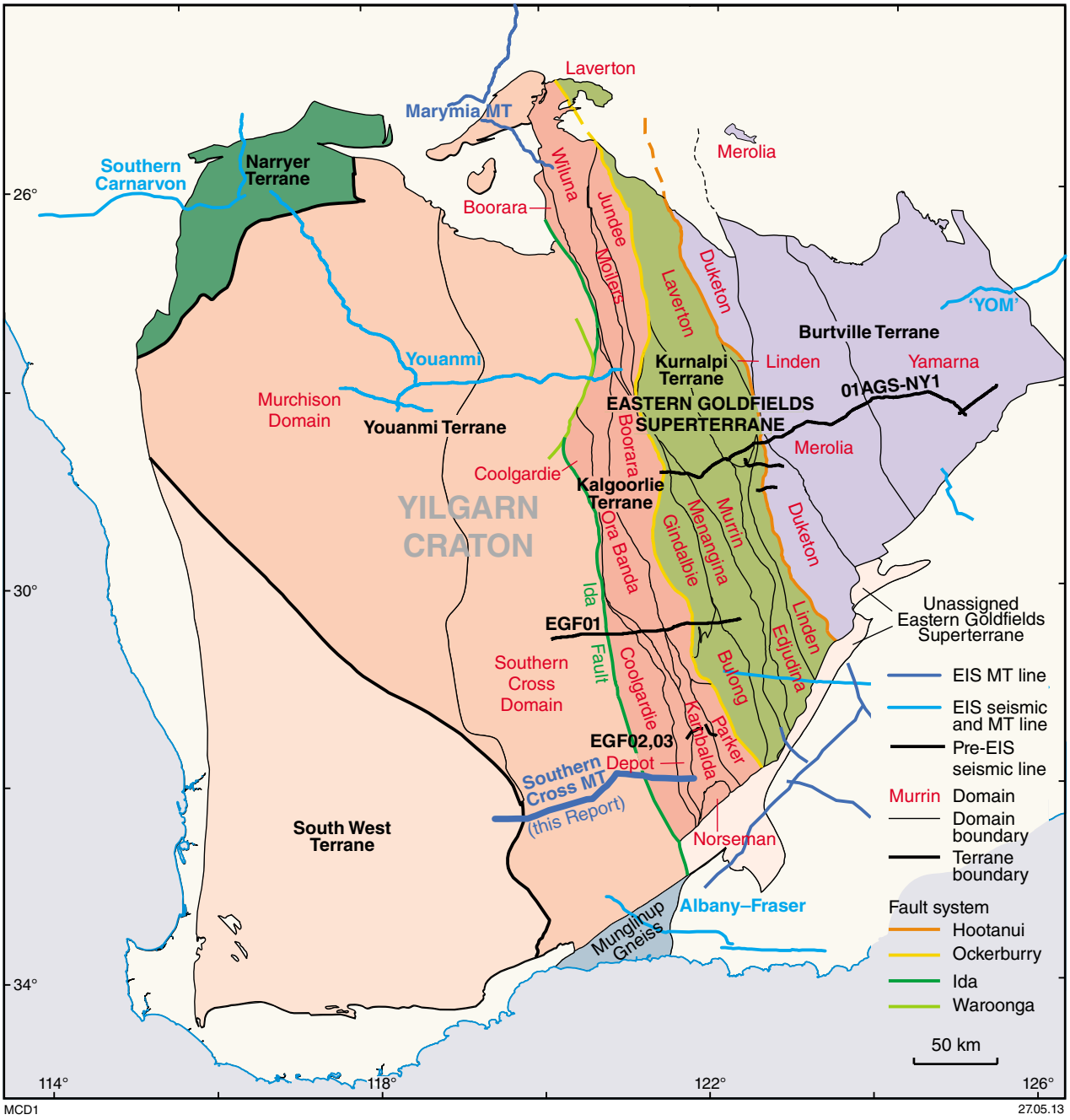

Figure 1. **Map of the Yilgarn Craton showing terrane and domain boundaries, the locations of the south Yilgarn MT traverse, and available previous seismic and MT survey data. Terrane names are in black, domain names in red. Geology from Cassidy et al. (2006). In the southern Yilgarn Craton, the Ida Fault marks the boundary between the Youanmi Terrane and the Eastern Goldfields Superterrane.**

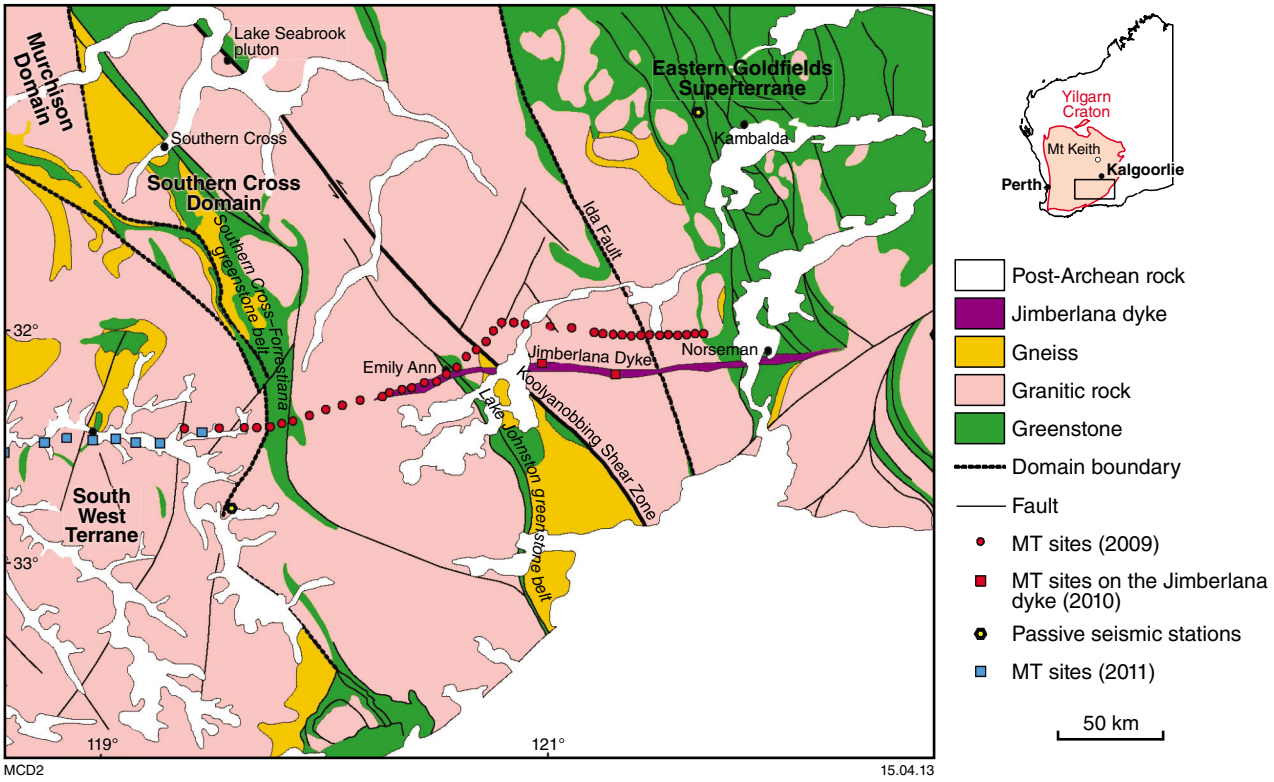

Figure 2. **Locations of MT stations overlain on regional geological map of the southern Yilgarn Craton showing major geological and structural boundaries, and the terranes and domains in this part of the craton. Note that the location of the Ida Fault, the boundary between the Southern Cross Domain and the Eastern Goldfields Superterrane, is not well constrained in this region. YC – Yilgarn Craton.**

Greenstones of the Youanmi Terrane are typically older than those of the Eastern Goldfields Superterrane (Cassidy et al., 2006). The style of granite magmatism across the Yilgarn Craton before c. 2660 Ma can be related to contemporary geological history in the greenstone successions (Van Kranendonk and Ivanic, 2009). After c. 2660 Ma, there was a craton-wide change in the style of granite magmatism from dominantly high-Ca granite to low-Ca granite (Cassidy et al., 2002).

The boundary between the South West and Youanmi Terranes is poorly defined (Wilde et al., 1996). In the east, the Ida Fault, which forms the boundary between the Youanmi Terrane and the Eastern Goldfields Superterrane, is a crustal-scale feature that has been imaged by deep-crustal seismic data (Drummond et al., 2000) and is clearly evident in aeromagnetic images and in chemical and isotopic character maps (e.g. Champion and Cassidy, 2007). The fault has been extensively intruded by late granites, particularly in the south. The MT survey also crosses the southern extension of the 6–14 km-wide, crustal-scale Koolyanobbing Shear Zone (Fig. 2; Libby et al., 1991). The maximum age constraint for deformation in the Koolyanobbing Shear Zone is provided by an age of c. 2699 Ma on a strongly deformed granodiorite, interpreted as a xenolith (Fletcher and McNaughton, 2002). The minimum age constraint of c. 2656 Ma is given by a post-kinematic granite (Qiu et al., 1999).

South West Terrane

The South West Terrane consists mainly of granite and high-grade granitic gneiss with subordinate supracrustal rocks, although it has been divided into three terranes on the basis of seismic data and the distribution of the various rock components (Wilde et al., 1996; Wilde, 2001). Granites and granitic gneisses range in age from c. 3280 Ma for the oldest gneisses in the west, to c. 2600 Ma elsewhere. The supracrustal rocks include at least two greenstone successions, one probably older than 3000 Ma — see Wilde (2001) for a review of the geochronology — and at least one younger succession, as exposed in the Saddleback greenstone belt near Boddington, aged between c. 2714 and c. 2670 Ma (Allibone et al., 1998).

Youanmi Terrane

The Youanmi Terrane is divided into the Murchison Domain in the west and the Southern Cross Domain in the east. The Lake Johnston and Southern Cross – Forrestania greenstone belts in the Southern Cross Domain host significant nickel and gold deposits.

Recent mapping in the Murchison Domain has identified at least four volcano-sedimentary successions (Van Kranendonk and Ivanic, 2009). The oldest successions,

the Golden Grove and Mount Gibson Groups are, as yet, poorly defined due to lack of recent regional mapping and geochronology in the western and southern Murchison Domain, but are known to contain substantial felsic volcanic components older than 2900 Ma (Yeats et al., 1996; Wang et al., 1998). The younger successions, which represent three broad ultramafic-to-felsic cycles, range in age from c. 2820 to 2700 Ma (Van Kranendonk and Ivanic, 2009).

Greenstone belts of the Southern Cross Domain consist predominantly of metavolcanic and metasedimentary rocks, but also include mafic to ultramafic sills and dykes. There are at least two greenstone successions: an older ultramafic–mafic–metasedimentary succession of unknown age, and a younger succession represented, for example, by c. 2730 Ma calc-alkaline volcanic rocks of the Marda Complex and clastic sedimentary rocks of the Diemals Formation (Chen et al., 2003). In the north of this region, quartzites in the Illaara and Maynard Hills greenstone belts have maximum depositional ages of c. 3130 Ma, and contain detrital zircons ranging in age up to c. 4350 Ma (Wyche et al., 2004). SHRIMP U–Pb ages indicate that parts of the greenstone belt successions in the Southern Cross and Lake Johnston greenstone belts, in the south of the Southern Cross Domain, are older than 2900 Ma (Wang et al., 1996; Mueller and McNaughton, 2000). Farther south, in the Ravensthorpe area, a c. 2966 Ma tonalite (Savage et al., 1996) and a c. 2958 Ma rhyolite from the upper greenstone succession in the Ravensthorpe greenstone belt (Nelson, 1995) indicate the presence of similarly old crust. The age and intimate spatial association of tonalite, tonalite porphyry dykes, and calc-alkaline volcanic rocks suggest a comagmatic relationship (Witt, 1997).

Southern Cross – Forrestania greenstone belt

The northerly trending Forrestania greenstone belt has a broadly synclinal structure. The lower part of the succession is predominantly mafic, but contains at least four sequences of komatiitic rocks that are intercalated with banded iron-formation (Perring et al., 1996). The upper part of the succession consists of clastic metasedimentary rocks (Chin et al., 1984).

The Southern Cross greenstone belt contains three successions. The lowermost unit comprises clastic metasedimentary rocks, and is unconformably overlain by a volcanic succession that is up to 5 km thick. Based on U–Pb zircon ages from porphyry sills from the Southern Star and Copperhead deposits, parts of the volcanic pile are interpreted to have formed before 2900 Ma (Mueller and McNaughton, 2000). A thick, unconformably overlying sedimentary succession has a maximum age of deposition of c. 2700 Ma (Thebaud and Miller, 2009), implying a major hiatus between the volcanic and sedimentary successions.

Lake Johnston greenstone belt

The Lake Johnston greenstone belt, which extends for about 100 km in a southeasterly direction, has been intruded by elongate granite bodies. The eastern side of the greenstone belt is transposed by the Koolyanobbing Shear Zone, whereas the northwesterly trending Tay Fault is a major structural feature on the western side of the belt.

The lowermost Maggie Hays Formation contains a thick package of submarine mafic volcanic rocks. Thin interflow metasediments become more abundant towards the top of the formation. The upper levels of the Maggie Hays Formation are intruded by sill-like, concordant to subparallel intrusions of the ultramafic–mafic Lake Medcalf Igneous Complex. The latter is geochemically distinct from the mafic extrusive rocks of the Maggie Hays and uppermost Glasse Formations (Romano et al., in prep.). The Honman Formation, which overlies the Maggie Hays Formation, changes upwards from felsic volcanic to metasedimentary rocks. There are intrusive and extrusive Barberton-type komatiites, now called the Roundtop Komatiite (Romano et al., in prep.), within and above the Honman Formation (Buck et al., 1998; Heggie, 2010; Fiorentini et al., 2011). Porphyritic intermediate volcanic rocks from the Honman Formation yielded zircon ages of c. 2921 and c. 2903 Ma (Wang et al., 1996). However, felsic volcaniclastic rocks overlying the intermediate volcanic rocks have a maximum depositional age of c. 2870 Ma (Thebaud et al., 2009), implying a younger depositional age for the komatiites. The uppermost exposed formation, the Glasse Formation, is a submarine mafic succession.

Isolated greenstone remnants

Isolated greenstone remnants that are exposed within metagranitic rocks between the Forrestania and Lake Johnstone greenstone belts include metamorphosed clastic sedimentary rocks, metamorphosed banded-iron formation, amphibolites, and undifferentiated metakomatiites.

Eastern Goldfields Superterrane

The Eastern Goldfields Superterrane is made up of four tectonostratigraphic terranes. From southwest to northeast these are the Kalgoorlie, Kurnalpi, Burtville, and Yamarna Terranes (Cassidy et al., 2006; Pawley et al., 2009). It hosts highly mineralized, elongate belts of deformed and metamorphosed, volcanic and intrusive, felsic, mafic, and ultramafic rocks, and metasedimentary rocks that range in age from 2958 to 2650 Ma (Nelson, 1997; Kositcin et al., 2008; Wingate and Kirkland, 2010). Supracrustal rocks have been intruded by abundant granitic rocks.

The Norseman–Wiluna greenstone belt in the Kalgoorlie Terrane is the most nickel-sulfide enriched komatiite belt in the world. The basal sequence is formed by the allochthonous c. 2930 Ma Penneshaw Formation, which comprises basal basic volcanic rocks that are unconformably overlain by chemical sediments. These are overlain by the <2684 Ma sedimentary rocks of the Noganyer Formation. The Woolyeenyer Formation contains mafic and minor sedimentary rocks, and komatiites (Doepel, 1973; McGoldrick, 1993; Krapež et al., 2000). A dolerite sill has been dated at c. 2720 Ma (Hill et al., 1992) and is unconformably overlain by the

felsic volcanic–volcaniclastic Mount Kirk Formation (Kositcin et al., 2008).

Granites

Granites in the South West and Youanmi Terranes have emplacement ages from c. 2750 to 2620 Ma, although most are younger than 2690 Ma (Nemchin and Pidgeon, 1997; Van Kranendonk and Ivanic, 2009). There are extensive migmatite bodies of unknown age between the Forrestania and Lake Johnston greenstone belts. Towards the north, the amount of monzogranite increases and migmatites disappear. A monzogranite intruding the western margin of the Lake Johnston greenstone belt yielded a zircon age of c. 2770 Ma (Romano et al., 2010), whereas granodiorites and monzogranites in the centre of the greenstone belt were emplaced at c. 2718 Ma (Romano et al., 2010).

East of the Lake Johnston greenstone belt and the Koolyanobbing Shear Zone, NNW-trending, strongly aligned, synkinematic, c. 2660 Ma porphyritic monzogranites (Hill et al., 1989; Hill and Campbell, 1993) are distributed over an extensive area. However, most of the granites in the Southern Cross Domain are at the younger end of the age spectrum. Granites older than c. 2730 Ma are rare (Wingate and Kirkland, 2010). Many of the granites in the Eastern Goldfields Superterrane contain inherited zircon populations as old as c. 3196 Ma, which is consistent with Nd-isotopic data that indicate that older crust must have been present (Hill et al., 1989; Champion and Cassidy, 2007).

Proterozoic

During the Paleoproterozoic, post-cratonization intrusions of easterly trending dyke swarms are represented in the southern Yilgarn Craton by the ultramafic to mafic Widgiemooltha Dyke Suite (Sofoulis, 1966), which intruded at c. 2410 Ma (Wingate, 2007). The Jimberlana dyke, one of the largest members of the Widgiemooltha Dyke Suite, lies parallel to the MT line east of the Koolyanobbing Shear Zone (Fig. 2).

Metamorphism

Granulite-facies metamorphism in the South West Terrane was synchronous with emplacement of c. 2640–2620 Ga charnockitic granites (Nemchin et al., 1994). However, metamorphism in the Southern Cross Domain is poorly constrained. Joly et al. (2010) described metamorphism at c. 2620 Ma for the Lake Johnston greenstone belt, which coincided with hydrothermal fluid flow in the Murchison Domain and northern Southern Cross Domain (Yeats et al., 1996; Mueller and McNaughton, 2000).

Detailed studies in the Eastern Goldfields Superterrane by Goscombe et al. (2009) identified localized high-pressure metamorphism until c. 2685 Ma. From c. 2685 to 2664 Ma, lower pressure metamorphism was related to extensive granite intrusion. After c. 2665 Ma, low pressure metamorphism and high heat flow was related to regional extension and the development of clastic sedimentary basins. This was followed by local alteration events, which have also been identified also in the broader Yilgarn Craton.

Magnetotelluric survey

Data acquisition

Data of the south Yilgarn MT survey were collected in three campaigns by personnel from Moombarriga Geoscience and the Centre for Exploration Targeting at the University of Western Australia. Most of the data were collected in the first campaign (October 2009), during which 40 MT datasets were recorded. The second campaign (March–April 2010) involved collection of eight MT datasets. These data were recorded to:

- supplement data from stations from the first campaign, for which original recording intervals were too short (5 sites)
- provide additional data for those parts of the traverse where an initial interpretation showed major variations in electrical structure (1 site)
- test the possibility that the Jimberlana dyke was influencing the data (2 sites).

In addition, during the second campaign, time-domain electromagnetic soundings were made at each MT station. A third campaign (December 2011) collected a further eight sets of MT data, but without associated electromagnetic soundings. These data were acquired to extend the survey westward to better define variations in deep electrical structure defined by the earlier data. Coordinates for all the MT stations are given in Table 1.

Figure 3 provides a schematic illustration of the equipment layout at each MT station. Two horizontal components of the electric field, and three components of the magnetic field, were measured at each site for approximately 40 hours. Data were recorded using Phoenix Ltd MTU-5A data recorders with MTC-50 magnetic induction coils. The coils were buried to mitigate their sensitivity to noise, a significant task, especially for the 2-m-long vertical coils. Electric dipoles (~100 m long) and horizontal coils were installed on magnetic north–south and east–west azimuths. The electric field was measured using non-polarising Pb/$PbCl_2$ solution electrodes. These consist of a container with a porous base, filled with electrolyte solution, which provides electrical contact with the ground. All survey sites were reasonably flat and most were remote from anthropogenic sources of electromagnetic noise.

Electromagnetic soundings were made using a TerraTEM transmitter and receiver. A square 100 × 100 m transmitter loop (Tx area = 10 000 m^2) was used with sides oriented north–south and east–west. The receiver coil had a 1-m side length (Rx area=105 m^2). The TerraTEM 'intermediate' time series was used (135 channels between

Table 1. Locations and recording times of MT stations

Site	Latitude	Longitude	Elevation (m)	Start time	End time	Duration (h)
Campaign 1						
STY001A	-32:25:09.66	+119:22:29.40	355	09/10/2009 7:00	11/10/2009 1:25	42.4
STY002A	-32:24:59.58	+119:31:51.54	366	09/10/2009 4:09	11/10/2009 0:42	44.6
STY003a	-32:24:52.92	+119:38:24.18	369	09/10/2009 2:07	10/10/2009 0:40	22.6
STY004a	-32:24:51.36	+119:42:06.12	415	08/10/2009 9:44	10/10/2009 0:05	38.3
STY005a	-32:24:47.76	+119:45:32.64	390	10/10/2009 2:50	12/10/2009 0:32	45.7
STY006A	-32:23:51.42	+119:48:38.16	394	10/10/2009 5:00	12/10/2009 0:59	44.0
STY007A	-32:23:11.22	+119:51:30.30	397	11/10/2009 4:30	13/10/2009 0:30	44.0
STY008A	-32:21:48.66	+119:56:03.60	422	11/10/2009 6:15	13/10/2009 1:03	42.8
STY009A	-32:20:15.06	+120:00:26.88	411	12/10/2009 4:00	14/10/2009 0:20	44.3
STY010A	-32:19:12.96	+120:05:00.36	432	12/10/2009 4:45	14/10/2009 0:51	44.1
STY011A	-32:17:51.90	+120:09:42.18	367	13/10/2009 6:00	14/10/2009 23:52	41.9
STY012A	-32:16:47.40	+120:14:30.78	344	13/10/2009 6:00	15/10/2009 0:29	42.5
STY013A	-32:15:51.42	+120:17:27.72	335	14/10/2009 5:50	15/10/2009 23:34	41.7
STY014A	-32:15:11.10	+120:20:55.68	356	14/10/2009 5:30	16/10/2009 0:06	42.6
STY015A	-32:14:32.40	+120:23:38.16	343	15/10/2009 3:00	16/10/2009 23:47	44.8
STY016A	-32:13:18.72	+120:27:04.26	352	15/10/2009 4:20	17/10/2009 0:16	43.9
STY017A	-32:13:06.00	+120:30:22.44	357	16/10/2009 6:00	17/10/2009 17:31	35.5
STY018A	-32:10:55.62	+120:32:53.28	351	16/10/2009 5:00	17/10/2009 17:10	36.2
STY019A	-32:09:22.74	+120:35:36.48	340	17/10/2009 2:20	19/10/2009 3:27	49.1
STY020A	-32:06:35.76	+120:38:06.96	347	17/10/2009 4:00	19/10/2009 1:12	45.2
STY021A	-32:04:46.74	+120:40:59.64	339	18/10/2009 5:38	19/10/2009 23:44	42.1
STY022A	-32:02:37.62	+120:43:22.98	347	18/10/2009 5:00	20/10/2009 0:21	43.4
STY023A	-31:59:51.12	+120:45:33.66	313	19/10/2009 7:00	20/10/2009 23:52	40.9
STY024A	-31:57:39.48	+120:47:47.64	314	19/10/2009 7:55	20/10/2009 22:39	38.7
STY025A	-31:58:11.04	+120:54:04.56	324	20/10/2009 4:00	21/10/2009 16:30	36.5
STY026A	-31:58:51.96	+121:00:51.06	351	20/10/2009 5:40	22/10/2009 0:47	43.1
STY027A	-31:59:09.72	+121:06:42.96	330	21/10/2009 2:40	22/10/2009 4:20	25.7
STY028A	-32:00:22.92	+121:12:49.38	330	21/10/2009 6:00	23/10/2009 1:57	44.0
STY029A	-32:00:41.22	+121:15:09.18	368	22/10/2009 7:00	23/10/2009 6:29	23.5
STY030A	-32:00:49.56	+121:17:52.08	316	23/10/2009 8:17	24/10/2009 1:18	17.0
STY031A	-32:01:06.48	+121:20:16.44	310	23/10/2009 5:00	24/10/2009 16:34	35.6
STY032A	-32:01:16.38	+121:22:48.24	319	23/10/2009 6:00	25/10/2009 0:44	42.7
STY033A	-32:01:05.82	+121:25:17.46	313	24/10/2009 4:00	25/10/2009 3:24	23.4
STY034A	-32:01:02.82	+121:27:37.74	356	25/10/2009 5:00	26/10/2009 0:11	19.2
STY034A	-32:01:00.78	+121:30:27.06	375	25/10/2009 9:00	27/10/2009 1:37	40.6
STY036A	-32:00:56.70	+121:32:41.16	387	25/10/2009 9:20	26/10/2009 21:32	36.2
STY037A	-32:01:07.20	+121:35:12.18	323	27/10/2009 2:00	28/10/2009 0:44	22.7
STY038A	-32:00:55.44	+121:37:40.08	302	27/10/2009 8:00	29/10/2009 0:37	40.6
STY039A	-32:00:46.44	+121:39:51.24	274	27/10/2009 8:30	29/10/2009 0:01	39.5
STY040A	-32:00:44.52	+121:42:11.94	280	28/10/2009 9:30	29/10/2009 2:06	16.6
Campaign 2						
STY003B	-32:24:53.04	+119:38:24.48	373	29/03/2010 5:00	31/03/2010 1:27	44.5
STY004B	-32:24:51.48	+119:42:06.42	418	29/03/2010 6:00	31/03/2010 2:20	44.3
STY018B	-32:10:55.92	+120:32:53.10	346	31/03/2010 9:00	01/04/2010 23:01	38.0
STY024-5	-31:57:48.12	+120:50:56.34	309	02/04/2010 2:00	04/04/2010 0:24	46.4
STY025B	-31:58:11.28	+120:54:04.50	324	01/04/2010 2:20	02/04/2010 1:34	23.2
STY026B	-31:58:51.84	+121:00:51.18	359	02/04/2010 3:34	04/04/2010 1:03	45.5

Table 1. continued

DT026A*	-32:08:25.44	+120:58:49.86	381	04/04/2010 8:00	06/04/2010 1:06	41.1
DT030A*	-32:11:04.74	+121:18:28.56	361	04/04/2010 6:00	06/04/2010 0:28	42.5
Campaign 3						
STYE01	-32:29:51.90	+118:33:51.06	298	20/12/2011 5:15	21/12/2011 5:35	24.3
STYE02	-32:27:24.90	+118:44:17.34	310	20/12/2011 6:45	22/12/2011 0:08	41.4
STYE03	-32:26:22.68	+118:49:36.54	323	20/12/2011 3:45	21/12/2011 4:41	24.9
STYE04	-32:27:38.34	+118:56:49.56	301	20/12/2011 8:36	21/12/2011 2:35	18.0
STYE05	-32:27:51.00	+119:03:02.40	330	19/12/2011 1:15	20/12/2011 7:16	30.0
STYE06	-32:27:47.58	+119:08:58.14	301	18/12/2011 10:30	20/12/2011 0:57	38.5
STYE07	-32:27:48.66	+119:15:21.12	324	18/12/2011 9:00	20/12/2011 0:29	39.5
STYE08	-32:24:53.70	+119:26:46.08	356	18/12/2011 7:00	19/12/2011 23:35	40.6

Note: * Station located on Jimberlana dyke

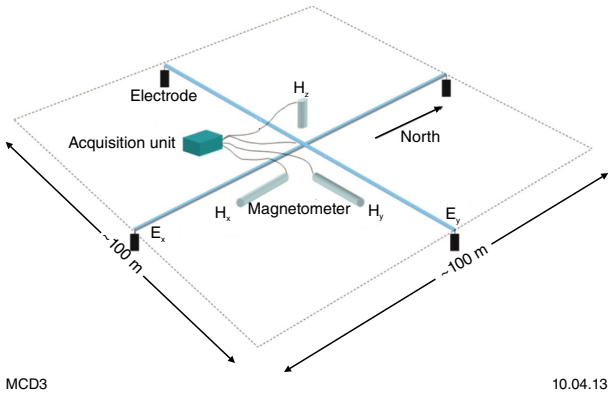

Figure 3. Schematic illustration of equipment setup at MT stations. *E* – electric field sensor, *H* – magnetic field sensor

0.0015 and 1900 ms). A minimum of four soundings were made at each site and visually checked for consistency and noise. Additional soundings were made if necessary.

Data processing

Variations of the electric and magnetic field components are recorded as a function of time (i.e. in the time domain). The MT data are subsequently converted to the frequency domain. This enables parameters of interest to be calculated as a function of frequency (or period) and then used to model variations of electrical properties as a function of depth.

Examples of partial electric and magnetic field time series recorded at two stations are shown in Figure 4. These series can be checked in the field to ensure that there has been enough variation in the geomagnetic field for the data to be useful, and also to check that the equipment has been deployed correctly, as can be determined by the relationships between the various time series. Electric field measurements are designated E. The north–south component is termed E_x and the east–west component E_y. Magnetic field components are designated H, with the same subscript notation, plus H_z to define the vertical component.

The time-series data were processed using robust remote-reference algorithms supplied by Phoenix Limited, based on the coherence-sorted cascade decimation method of Wight and Bostick (1981) and the heuristic robust approach of Jones and Jödicke (1984). Remote-reference processing (Gamble et al., 1979) compares recordings from different locations to identify noise in the time series, whereas coherence-based methods are based on statistical comparison of the various time series. A simultaneously recording station within the traverse was used as the remote reference.

Frequency-domain MT responses

Figure 5 presents the same datasets as shown in Figure 4 after transformation to frequency domain. Two parameters, apparent electrical resistivity (ρ or rho) and phase, are shown as a function of period. Note that electrical resistivity is the reciprocal of electrical conductivity.

In general, data quality from the south Yilgarn MT survey is very good, as indicated by the small errors bars in Figure 5, up to periods of about 1000 s. However, one station (STY040) was rejected as too noisy. A complete set of apparent resistivity and phase curves is provided in Appendix 1.

The apparent resistivity values for each period were calculated as follows. Apparent resistivity can be written in terms of the electric (E) and magnetic (H) fields as:

$$\rho = \frac{1}{\omega\mu}\left|\frac{E}{H}\right|^2 \qquad \text{Equation 1}$$

where $\omega = 2\pi f$ is the angular frequency of the fields and

μ is the magnetic permeability of the Earth. The ratio of the two fields is the impedance ($Z = E/H$), a measure of the opposition to the flow of alternating electric currents. As shown by equation 1, apparent resistivity is related to the square of impedance.

The MT impedance tensor contains four complex-valued transfer functions (Z_{xx}, Z_{xy}, Z_{yx}, Z_{yy}) between the various orthogonal components of the horizontal electric and magnetic fields (equation 2). Each MT impedance term can be used to estimate an apparent resistivity, a volumetrically averaged resistivity over the penetration depth of the signals.

$$\begin{bmatrix} Z_{xx} & Z_{xy} \\ Z_{yx} & Z_{yy} \end{bmatrix} \begin{bmatrix} H_x \\ H_y \end{bmatrix} = \begin{bmatrix} E_x \\ E_y \end{bmatrix} \qquad \text{Equation 2}$$

If the Earth's electrical structure is one-dimensional (1D; i.e. is a horizontally layered structure) or two-dimensional (2D), with the x- and y-directions parallel and perpendicular to strike respectively, then $Z_{xx} = Z_{yy} = 0$. If the strike is known, the data can be rotated accordingly, in which case the non-zero Z_{xy} and Z_{yx} impedance can be used to determine apparent resistivity as a function of frequency according to equation 1, where ρ_{xy} is determined from E_x, H_y, and ρ_{yx} by using E_y and H_x (equation 3 and Fig. 5). After rotation, xy data are referred to as transverse electric (TE) mode, and yx data as transverse magnetic (TM). In TE mode the electric field is parallel to strike and the magnetic field is perpendicular to strike. In TM mode, the magnetic field is parallel to strike and the electric field is perpendicular to strike.

$$\rho_{xy} = \frac{1}{\omega\mu}\left|\frac{E_x}{H_y}\right|^2 \qquad \rho_{yx} = \frac{1}{\omega\mu}\left|\frac{E_y}{H_x}\right|^2 \qquad \text{Equation 3}$$

Also important is the phase difference (ϕ) between the two fields: $\phi = \arctan(E/H)$. The phase is defined as the lead of the electric field over the magnetic field.

Static corrections

MT data are prone to static shifts due to heterogeneous electrical properties in the near surface at scales smaller than the resolution of the MT data. Such static shifts are frequency-independent; that is, the entire apparent resistivity curve is shifted parallel to the apparent resistivity axis by an amount known as the static shift factor. Failure to account for this during data modelling will lead to incorrect estimation of resistivities and the depths at which they occur.

There are various approaches to account for static shift. For example the shift may be treated as an unknown variable in modelling of the data). For the south Yilgarn MT survey, static shifts were estimated by using the time-domain electromagnetic (TEM) soundings (where available). These data were inverse modelled to derive a two- or three-layered 1D earth model that was consistent with the observed time-domain data. This model was then used to forward model an MT response, which was compared with the observed MT data. The MT curves are translated so that they overlay the time-domain data (Fig. 6). To achieve this with accuracy requires the time-domain derived and MT data curves to overlap. This was generally the case. Figure 6 also illustrates a limitation of this approach. The TEM curve assumes a layered (1D) variation in electrical properties, but the separation of the two MT curves suggests the variation is more complex. Nevertheless, the approach is considered to be an improvement on having no information about near-surface variations of electrical properties.

All of the equivalent MT curves derived from time-domain soundings are provided in Appendix 1. The static shift factor dictates whether the apparent resistivity curves are moved up (s >1) or down (s <1). The mean xy static shift factor was 1.98, and that for yx data was 2.15.

Dimensionality and geoelectric strike

Most MT modelling algorithms assume the area of interest is geoelectrically either 1D or 2D. A 3D electrical structure requires greater computational power to model the data and the earth models must be comparatively simple. For the normal 2D modelling scenario, the direction of geoelectric strike is assumed to be consistent; that is, there should not be any localized or off-profile variations of geoelectrical properties, and the strike direction must be known. The frequency-dependent variations in impedance are also used to determine the electrical dimensionality and geoelectric strike direction of the subsurface.

Where there are lateral conductivity gradients within the Earth, vertical magnetic fields are created. Induction arrows are the vector representations of the complex ratios of the vertical to horizontal magnetic fields. Because these ratios are complex numbers, both real and imaginary induction arrows can be produced. In the Parkinson convention, real arrows point towards regions of low resistivity, or away from regions of high resistivity. The length of an arrow indicates the magnitude of the difference in resistivity. Where the electrical structure is 2D, the real arrows will be parallel to each other and oriented perpendicular to geoelectric strike. The dimensionality of the MT data was assessed using the phase-tensor method of Caldwell et al. (2004). Unlike many other methods used to estimate dimensionality, this method analyses only phase variations, because these are unaffected by galvanic distortion associated with near-surface changes in electrical conductivity, and because the method does not rely on assumptions that the regional electrical structure is 1D or 2D.

Three parameters are used to characterize the phase tensor: the maximum and minimum phase values, and the skew angle (β). The angle α is a measure of the tensor's orientation relative to the coordinate system and the ellipticity is a measure of the ratio of the maximum (Φ_{max}) and minimum (Φ_{min}) phase values. The phase tensor is commonly represented as an ellipse (Fig. 7) with the long and short axes of the ellipse representing the maximum and minimum phase values, respectively, and the orientation ($\alpha - \beta$) of the major axis representing

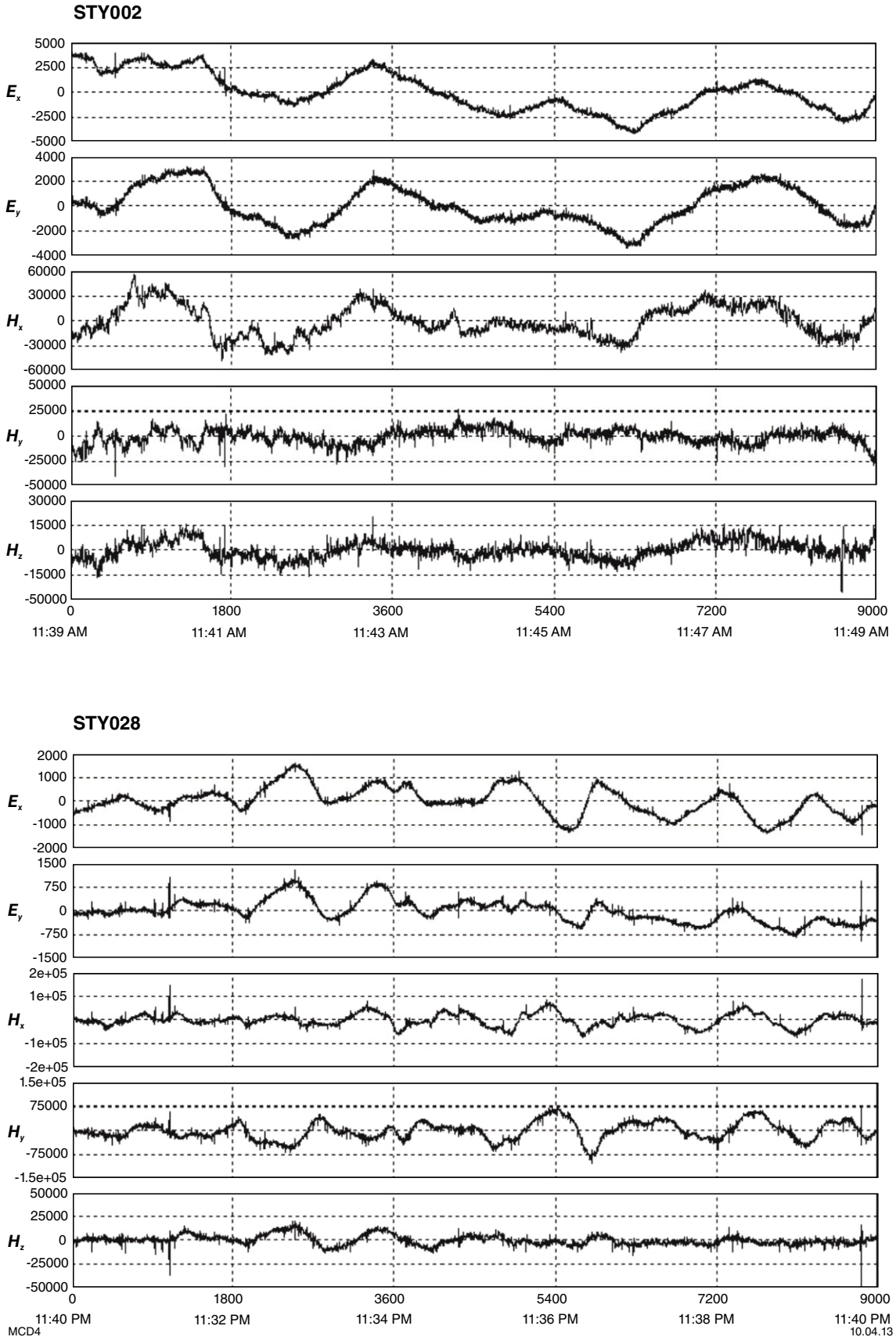

Figure 4. Examples of MT time series from two stations. Note the higher short-wavelength noise levels in STY002.

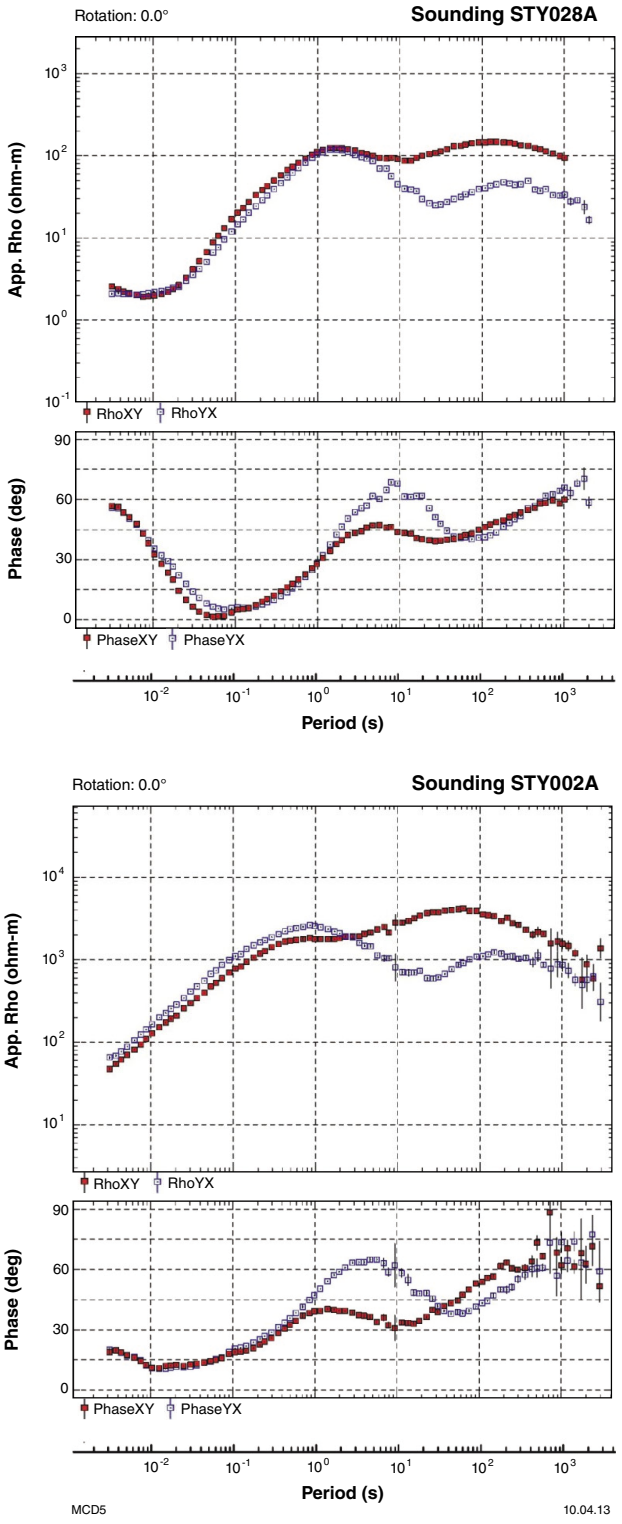

Figure 5. Examples of MT soundings from the two stations shown in Figure 4. Red symbols show the x–y response and blue symbols show the y–x response. Note the increased errors as the data approach the longest periods (greatest depths).

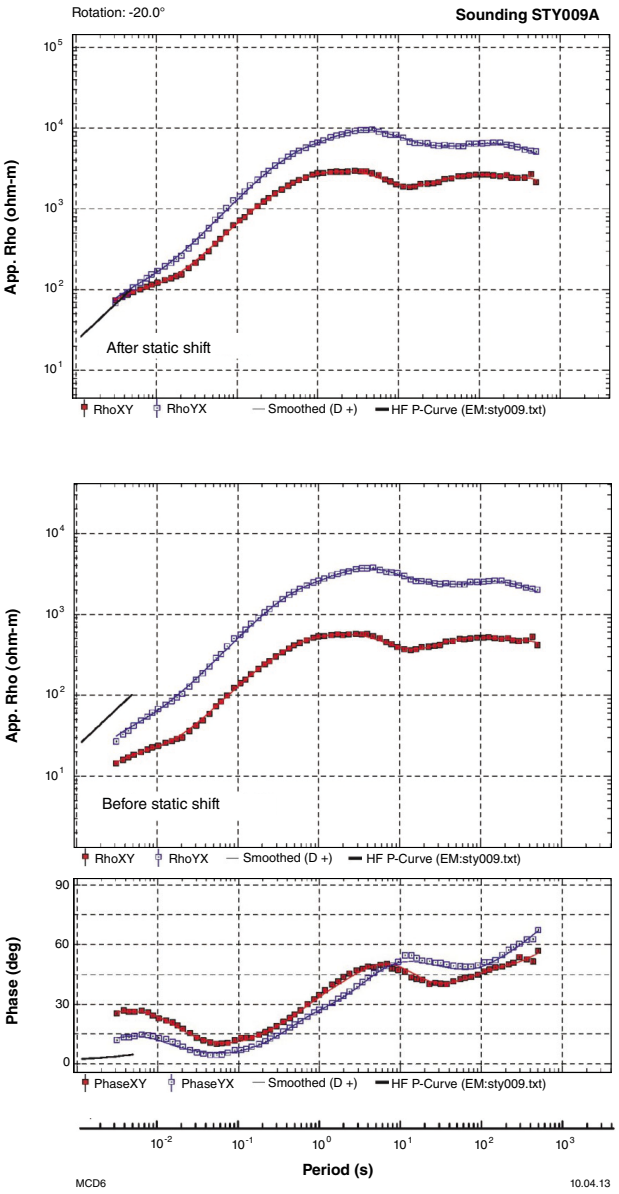

Figure 6. Example of correction for static shift (STY009). The solid line represents the MT response predicted from time-domain electromagnetic soundings. Note the shift of the apparent resistivity data to overlie this line after static correction of the data (top panel). The red symbols show the xy response and the blue symbols show the yx response. Static shift factors are 5.27 (xy) and 2.55 (yx).

the direction of maximum current flow. A 1D subsurface is represented by a circle. A 2D subsurface is represented by an ellipse. A 3D subsurface results in a skewed ellipse with the main axis deflected by an angle β from the axis of symmetry (dashed line in Figure 7).

Figure 8 shows phase-tensor ellipses and real induction arrows for each station of the south Yilgarn MT survey. Results for five periods are presented, ranging from 0.01 to 100 s (100 to 0.01 Hz). Shading is according to invariant minimum phase. Generally, phases <45° indicate a change with depth from conductive to more resistive rocks. If the phase is >45° then the change is from resistive to conductive rocks. Also plotted are real induction arrows following the Parkinson convention (i.e. arrows pointing towards conductive features).

Up to periods of 1 s (1 Hz), the minimum phases are small <25°, probably due to the effects of electrically conductive regolith overlying more resistive crust. The ellipse orientations change more rapidly, indicating a heterogeneous electrical structure. In places, the orientations of the phase-tensor ellipses flip through 90°, as expected where there are lateral conductivity gradients (Caldwell et al., 2004). This behaviour corresponds with known major fault structures, for example, at the boundary between the South West Terrane and the Southern Cross Domain. Across these zones, the induction arrows also tend to rotate by 180°, pointing towards the conductive structures. In areas lacking major faults, the induction arrows are generally smaller, suggesting a more electrically homogeneous crust.

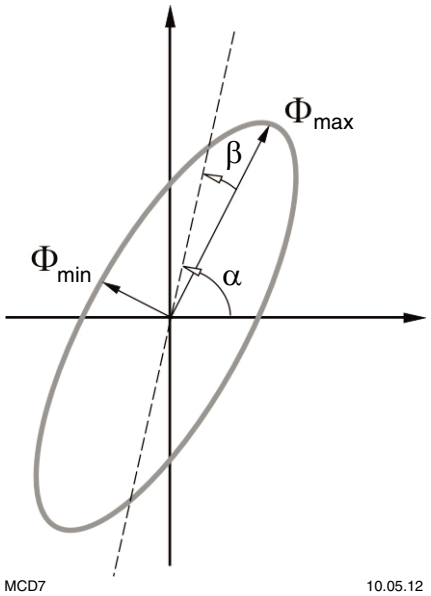

Figure 7. Graphical representation of the MT phase tensor illustrating the parameters used to define the phase ellipse (from Caldwell et al., 2004).

At longer periods (>1 s; <1 Hz) responses become more consistent across the traverse. Ellipse axes are oriented roughly north–south with induction arrows pointing more east–west (P = 10 s), suggesting that the main strike is more or less north–south at upper-crustal to mantle depths. At 100 s period, the ellipses become less elliptical and there is less variation in minimum phase values, indicating less of a preferred direction of current flow in a homogeneous upper mantle. The induction arrows tend to rotate to a uniform southeasterly orientation for long period. The Southern Ocean is approximately 180 km south of the MT traverse and may be responsible for this deflection of the induction arrows. Note that the study area is electrically complex around station STY024–25, which is why data were collected at an additional station (STY024.5) and stations STY025 and STY026 were re-occupied during campaign 2 of the survey (see Table 1).

Figure 9 shows phase-tensor and real induction arrows within a pseudosection presentation (a cross-sectional display where period is used as a pseudo-depth parameter). Empirically, a skew angle in the range $-5° < \beta < 5°$ means the data are predominantly 2D, such that ellipses coloured blue, red, and orange have significantly 3D characteristics. These areas also coincide with rapid changes in the orientations of both ellipses and induction arrows. The greatest changes in orientation, magnitude, and skew are seen at periods of around 1 s (frequency = 1 Hz). This probably reflects the transition from the heterogeneous near-surface responses around individual stations (with their own strike directions) to the more regional response at depth (the common strike direction of the profile for the structurally simpler lower crust and upper mantle).

Figure 10 presents rose diagrams showing strike direction calculated from phase-tensor ellipses. The mostly east–west orientation of the induction arrows indicates that the geoelectric strike is roughly north–south. Strike is undetermined for periods below 0.1 s (>10 Hz), but becomes more or less northerly for longer periods. In particular, for periods >1 s, strike is roughly 010°, shifting to >030° for periods >100 s.

The average strike direction calculated for campaign 1 and 2 data, with absolute skew <5°, is –2°. If periods between 1 s and 100 s only are considered (where there is a more dominant strike across the profile), the average strike direction is 010°. This is the strike direction that was used to model the data (see next section).

The northerly geoelectrical strike corresponds with the gross trend of the major geological structures of the eastern Yilgarn Craton (Fig.1). The main lithological and structural trend in the study area varies between north–south and northwest–southeast but the geoelectric strike does not reflect this variation (Fig. 2).

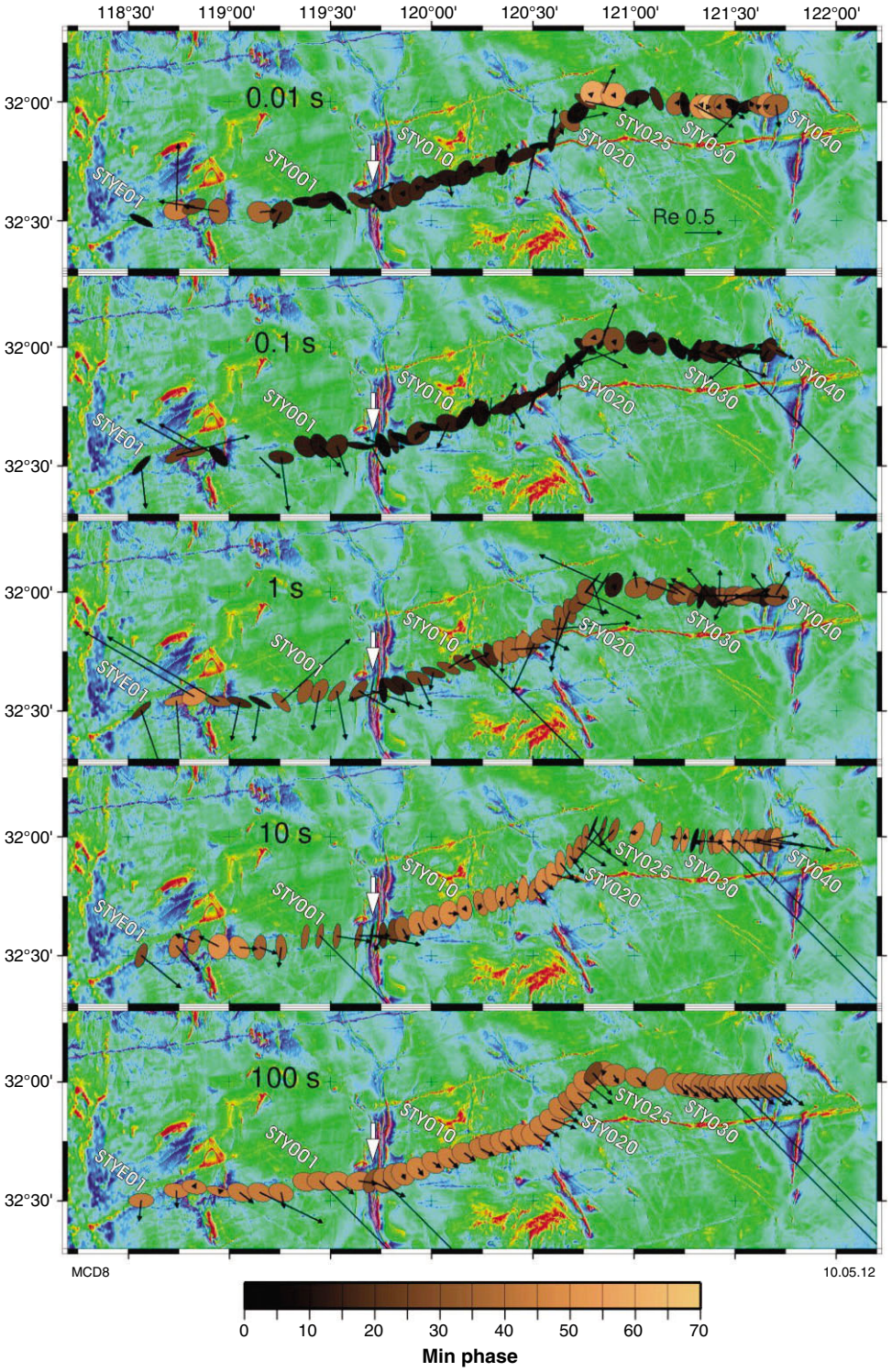

Figure 8. **Phase ellipses and induction arrows (black) for each MT station for five periods. The length of each black arrow indicates the magnitude (Re) of the difference in resistivity. In each panel, the white arrow indicates where the MT traverse crosses the surface boundary between the South West Terrane and the Southern Cross Domain.**

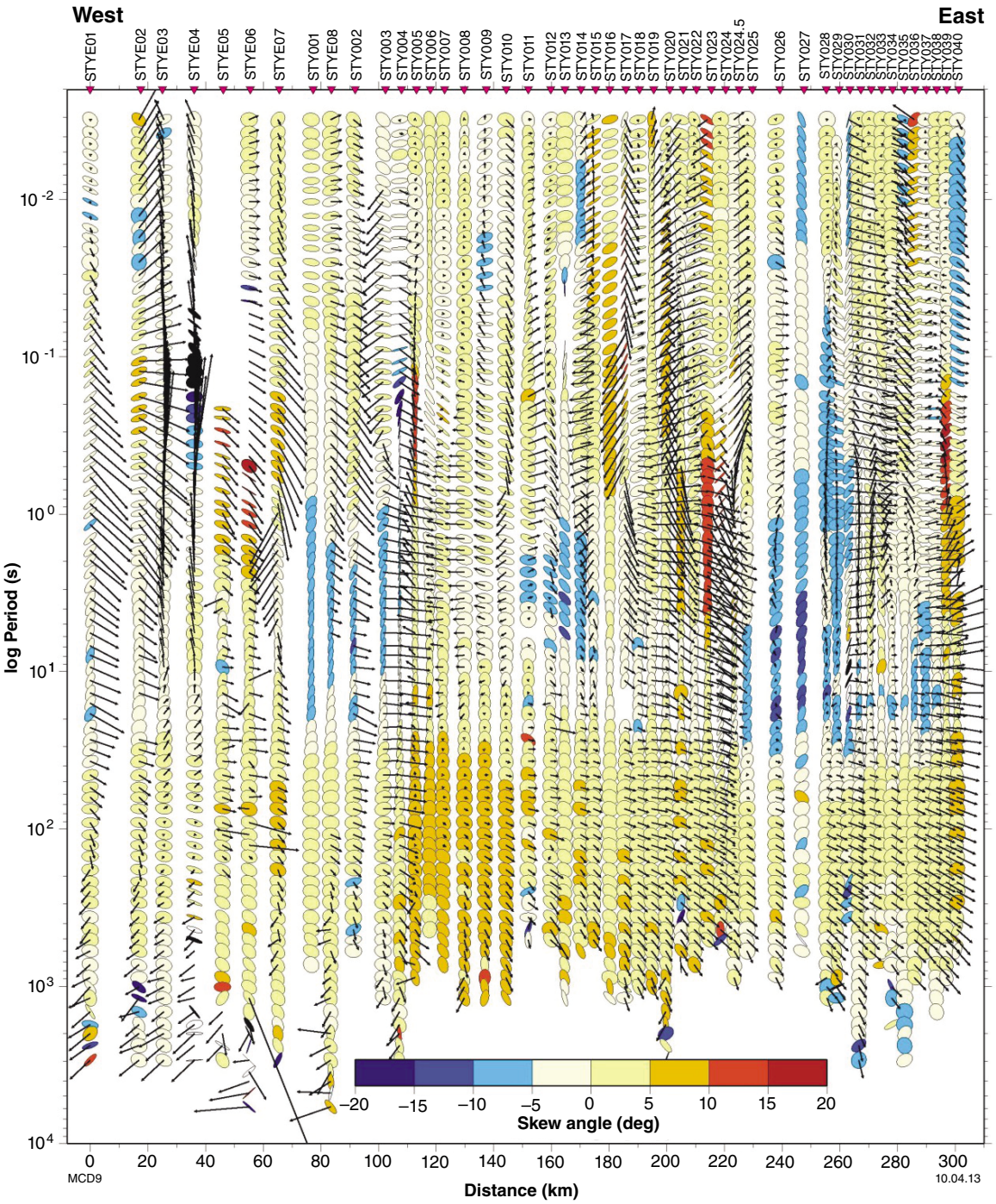

Figure 9. Pseudosection of MT phase-tensor data

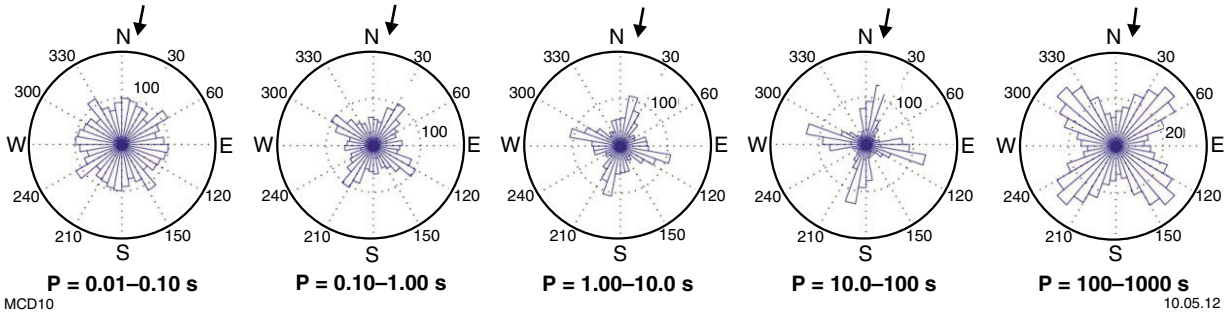

Figure 10. Rose diagrams of phase-tensor ellipse orientations. Black arrows show the geoelectric strike used for data modelling.

Data modelling

Figure 11 shows TM- and TE-mode pseudosections of apparent resistivity and phase for all data points judged to not be overly noisy. Figure 12 shows the equivalent pseudosections after removal of data affected by 3D conductivity variations (see Fig. 9); absolute skew is less than 5°. Note in particular the loss of data at a period of about 1 s; these are responses originating mostly from the upper-middle crust. In general, there is reasonable correlation between data from adjacent stations. Vertical streaking of the apparent resistivity data is likely due to incorrect estimation of static shifts. These effects are particularly evident in the campaign 3 data (station numbers prefixed STYE) at the western end of the traverse, where no TEM data were collected.

Effect of Jimberlana dyke

As noted above, the survey traverse is close to the Jimberlana dyke, a major Proterozoic intrusion that runs parallel to the eastern part of the MT traverse and about 20 km to the south. Initial data modelling of the campaign 1 data showed that the geometry of east-dipping features at the eastern end of the cross section was consistent with a response from the dyke; that is, the apparent depth of some conductivity variations appeared to mimic the distance to the dyke from the MT traverse. However, subsequent analysis showed that the influence of the dyke was negligible. In support of this conclusion are induction arrow directions, including those from stations located on the dyke.

Figure 13 shows induction arrows for MT sites of the main traverse and the two specially collected datasets from stations located on the Jimberlana dyke. If the dyke were strongly conductive, then the induction arrows for shorter periods would be expected to point towards the dyke, which is not the case. The short induction arrow at the westernmost station on the dyke is indicative of a conductive feature beneath the station but, overall, the data indicate that the dyke is not a large-scale conductive feature. Subsequent modelling of the MT dataset showed that conductivity variations are not consistent with an out-of-profile response from the dyke.

2D conductivity model

Data not significantly affected by 3D conductivity variations were modelled using the 2D non-linear conjugate gradient inversion algorithm of Rodi and Mackie (2001), as implemented in the WinGLink® software package (GEOSYSTEM SRL, 2008). This inverse modelling method minimizes an objective function consisting of the data misfit and a measure of model roughness, with the user-specified trade-off parameter, τ, defining the balance between these terms. TE and TM modes and the H_z transfer function were modelled over the frequency range 500 – 0.001 Hz using a uniform grid Laplacian operator and $\tau = 3$. Geoelectric strike was taken to be 010° (see above). Error floors are listed in Table 2. Error floors are typically chosen so that the values for apparent resistivity are twice those of the phase. When using the WinGLink inversion algorithm, this ensures that there is equal weighting from apparent resistivity and phase. For this inversion, a slightly larger relative error floor for the apparent resistivity was used to accommodate minor residual distortion and static effects. The slightly larger error floors for the TE mode account for the greater perturbation of the TE mode by 3D inductive effects.

Figure 14 shows the differences, in pseudosection form, between the observed data and the preferred calculated data associated with the 2D conductivity model. The misfit between observed and calculated data corresponds to an overall RMS difference of 4.5369. As expected, the fit to the TM data is better than to the TE data, because of the greater 3D influence on the TE response. There is some streakiness in the pseudosection data, suggesting that static effects have not been fully accounted for. The misfit of observed and calculated data, indicated in the graph at the top of Figure 14, is greater at the western end of the traverse (notably at stations STYE04–06), again possibly due to static effects. Alternative explanations are either an undefined effect due to the presence of salt lakes in this area, or failure to remove 3D responses such as those in the higher periods of these datasets.

The preferred 2D resistivity model is shown in Figure 15a (and duplicated in Fig. 15f,k,p). To assess the reliability of the resistivity model produced by the inversion, we tested various distinct conductive and resistive zones labelled A–H in Figure 15a,f,k,p in the cross section. First, the anomalies were selected on the basis of their perceived geological significance. In each case, the 'anomalous' zone (e.g. zone A in Fig. 15a) was removed and replaced with the conductivity of the immediately adjacent ('non-anomalous') area. For example, in the case of discrete conductive zones in the upper crust these are replaced with resistive values similar to those outside the feature being tested. The resistivity in the selected zone was then 'frozen' and the inversion process restarted. This forces the inversion algorithm to try to match the observations using conductivity variations from outside the anomalous zone. This test was designed to see whether conductivity variations elsewhere in the model could be used to fit the data. That is, does there needs to be a zone of anomalous conductivity in the zone being tested?

The type of feature second test allowed the modelling algorithm to modify values within the test zone (i.e. 'unfrozen' tests) to see if the anomalous zone reappeared and, if so, how its geometry was affected. This second test was less rigorous than the first in terms of the presence or absence of a feature, but allowed the reliability of a feature's geometry to be assessed (i.e. did it reappear in the same form as in the original model?). Table 3 lists the overall RMS misfit between model and observations after: (1) the feature is removed, (2) re-running the inversion with the area frozen, and (3) re-running the inversion with the area unfrozen.

Features A to E are all dipping conductive zones in the upper crust. As expected, removing these features increased the misfit. The slight increase associated with feature C probably reflects the poor fit to the data in this part of the model (Fig.14).

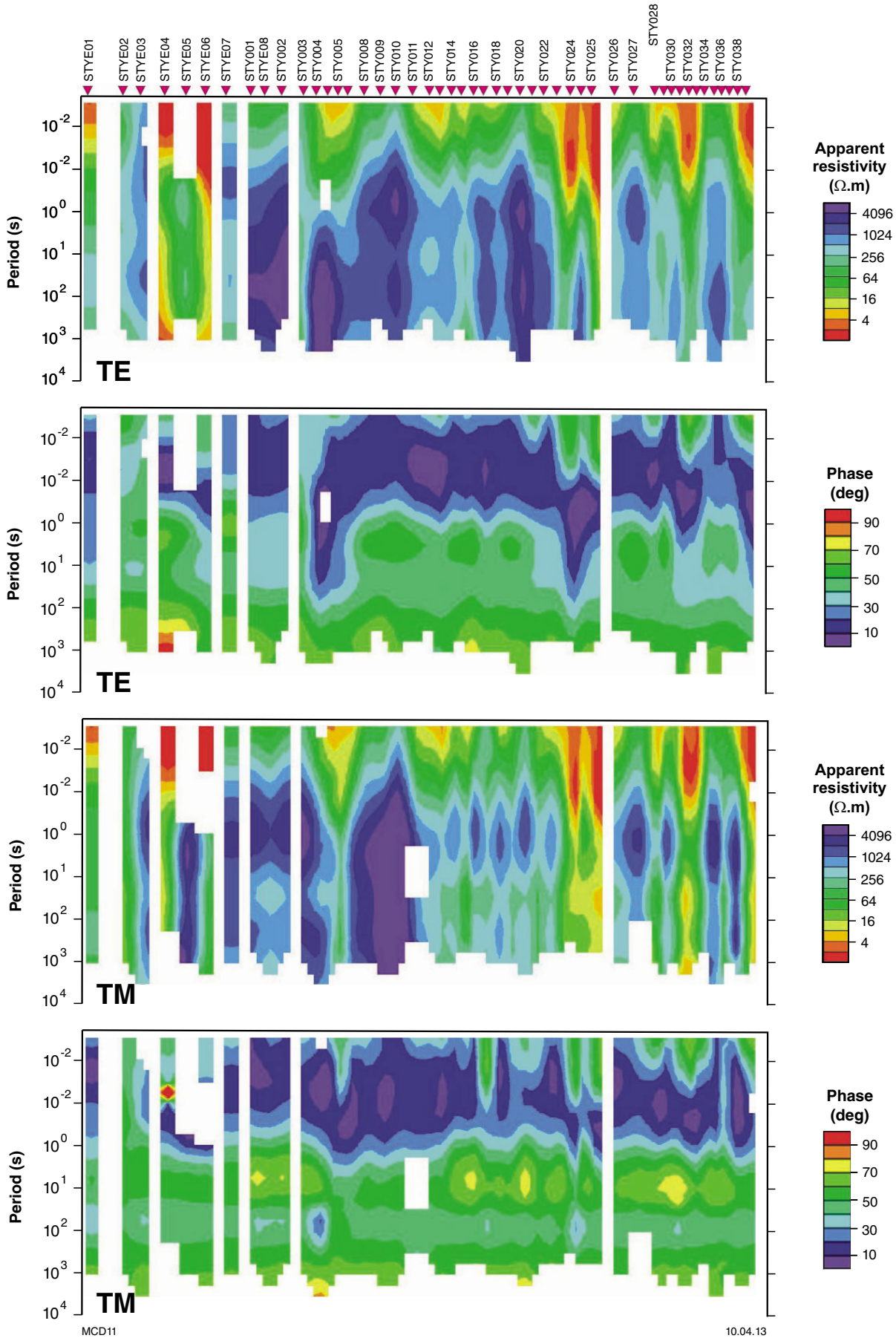

Figure 11. TE- and TM-mode pseudosections of data considered to have acceptable signal to noise ratios

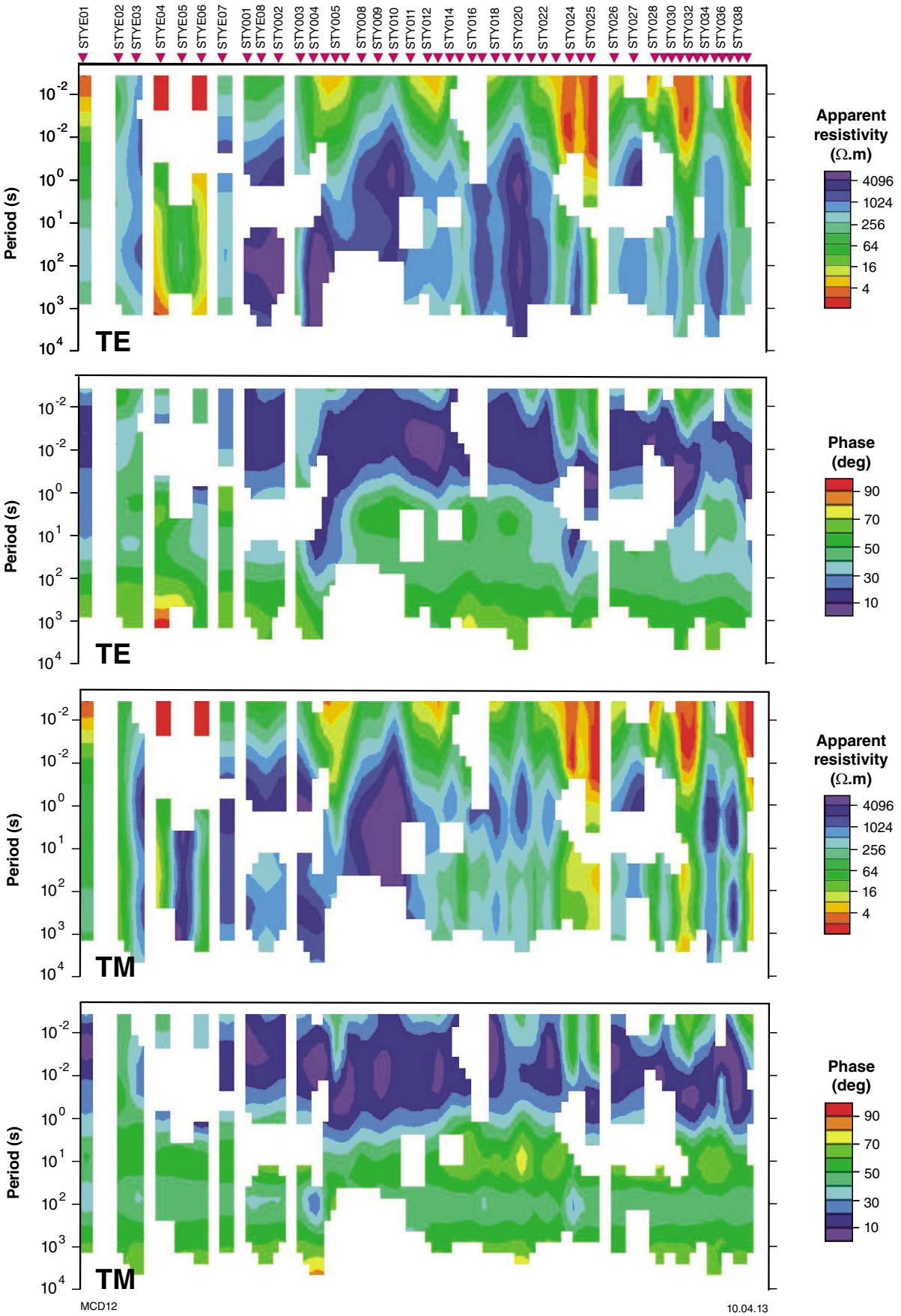

Figure 12. TE- and TM-mode pseudosections of data considered to have an acceptable signal to noise level and no significant 3D influence, as defined by skew (β) in the range –5° < β < 5°. These data were modelled to create the resistivity cross section in Figure 19.

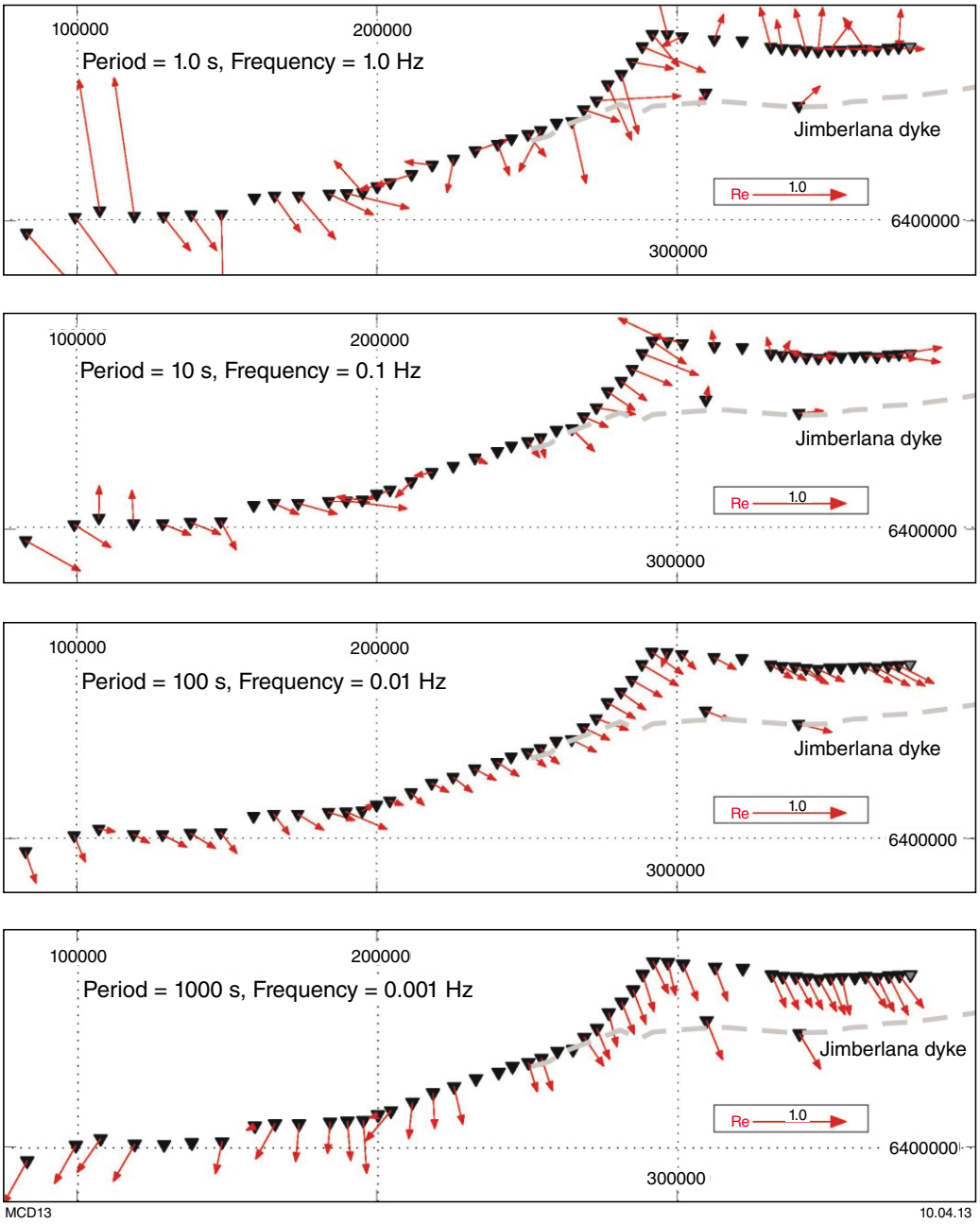

Figure 13. Induction arrows for different periods illustrating the influence from the Jimberlana dyke. Note that the arrows are not directed towards the dyke, indicating it is not a major conductor.

Table 2. Error floors used in 2D modelling

	TE mode	*TM mode*
Apparent resistivity	15	12.5
Phase	5	2.5
T_{yz} data	0.02	

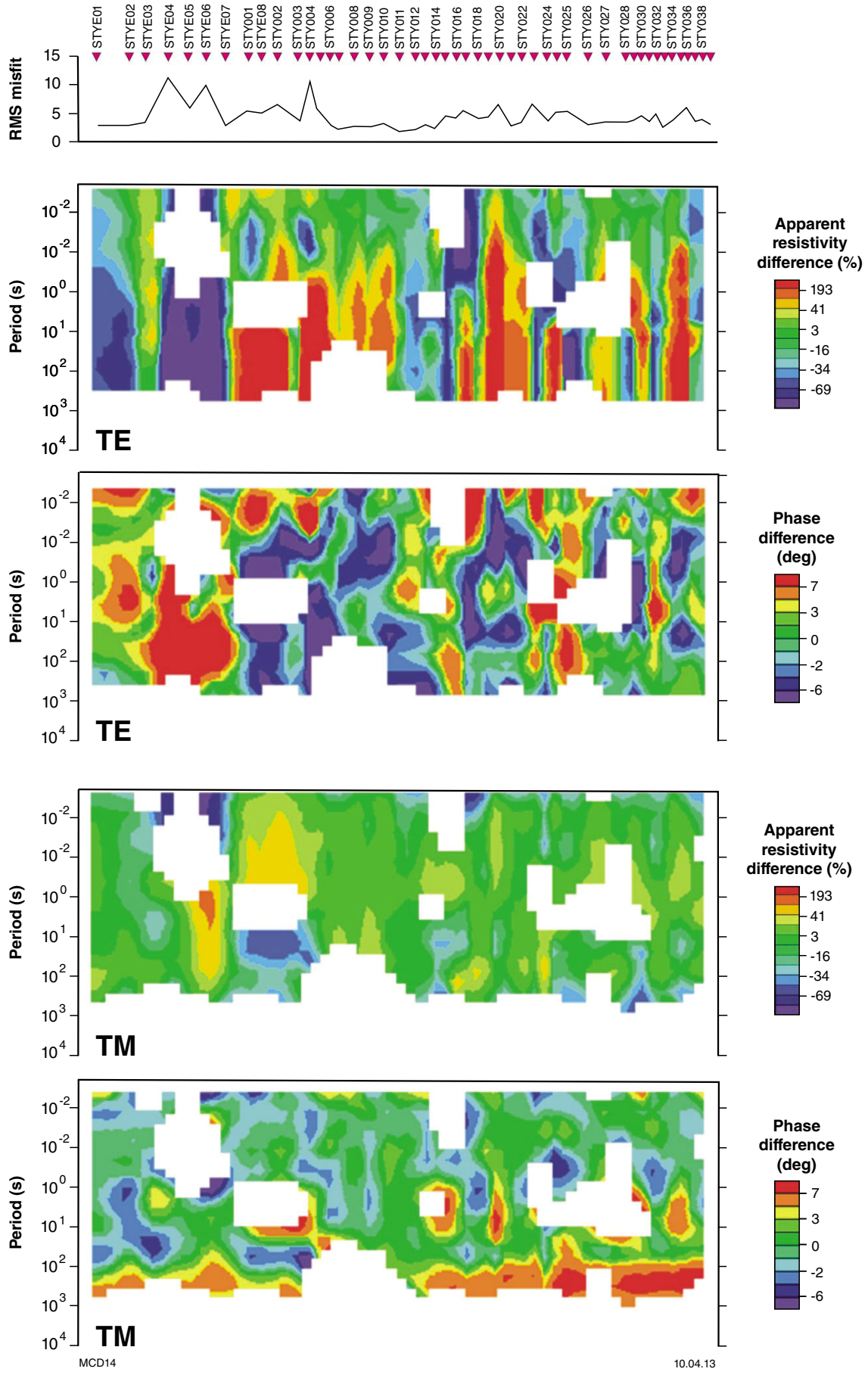

Figure 14. RMS misfit at each station, and pseudosections showing TE- and TM-mode differences between the observed data and the preferred model.

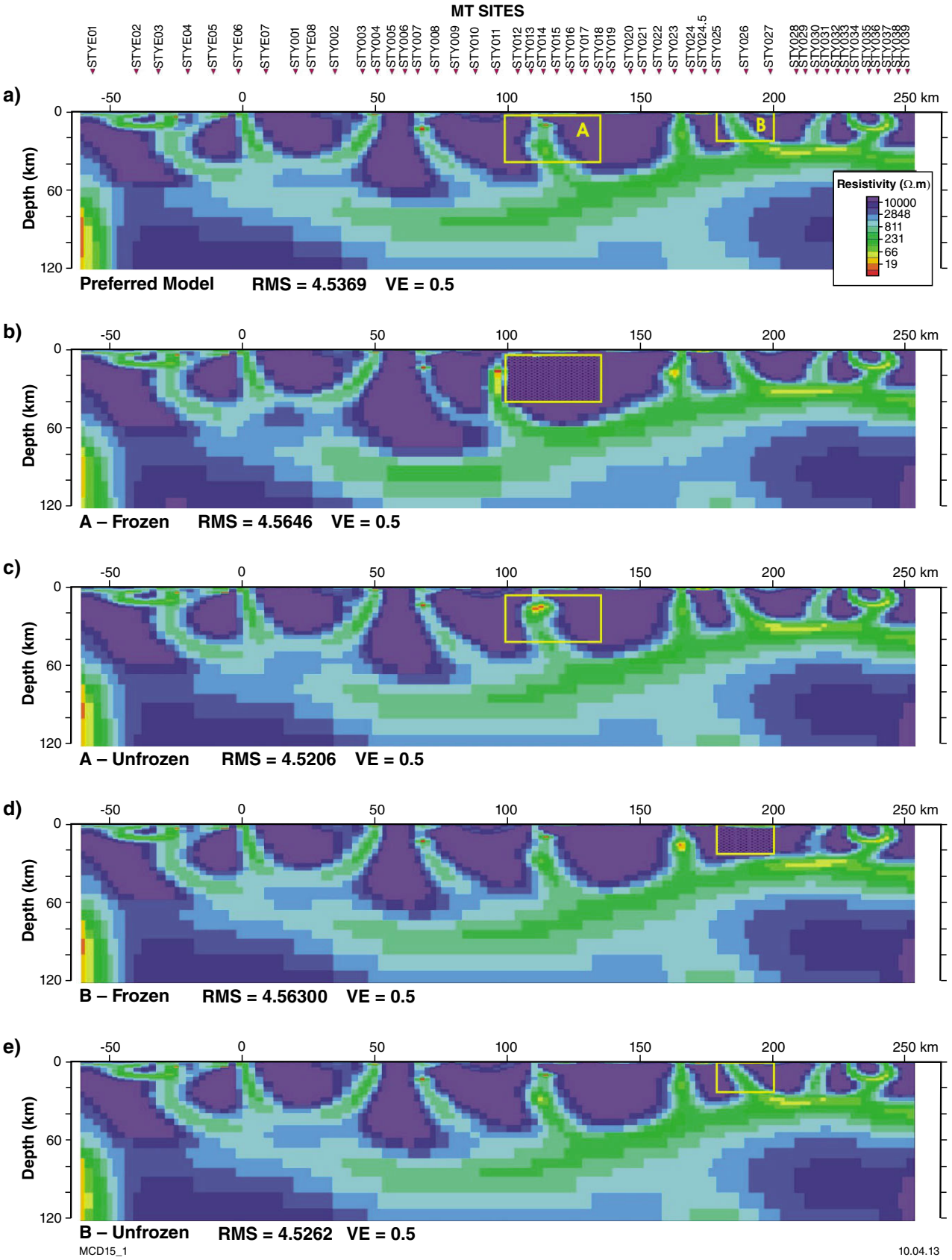

Figure 15. **Assessment of the reliability of features with anomalous electrical properties in the preferred resistivity cross section (parts a, f, k, and p). Each of the anomalous features (areas labelled A to H) was been removed and then re-modelled twice. Firstly, the area was 'frozen' to see if the data could be fitted with conductivity variations from other parts of the model. Secondly the data were re-modelled with the area 'unfrozen' to see if the feature of interest re-appeared; this was taken as evidence that the feature is required to correctly model the observed data. Vertical exaggeration = 0.5. See text for explanation of specific cross sections.**

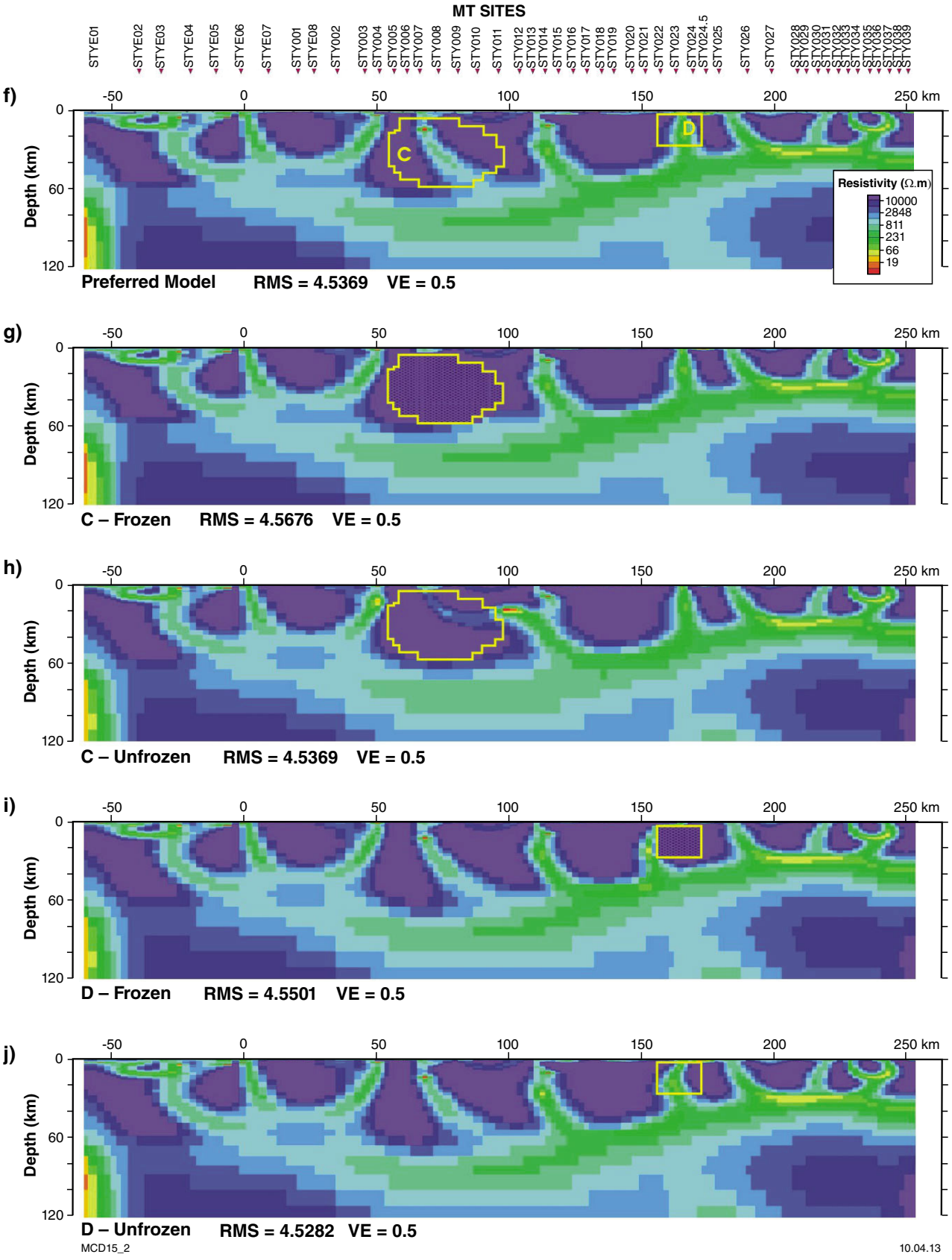

Figure 15. continued

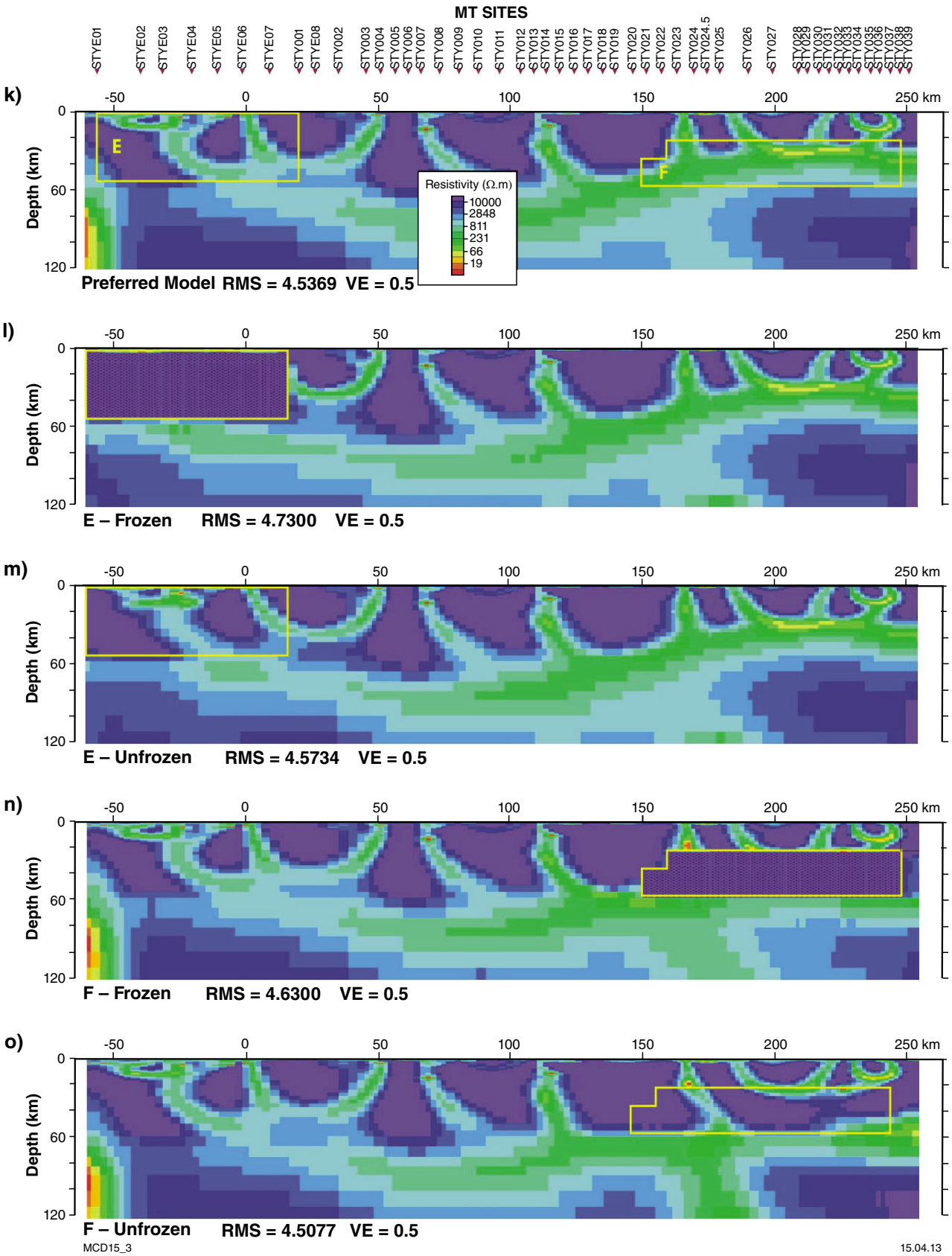

Figure 15. continued

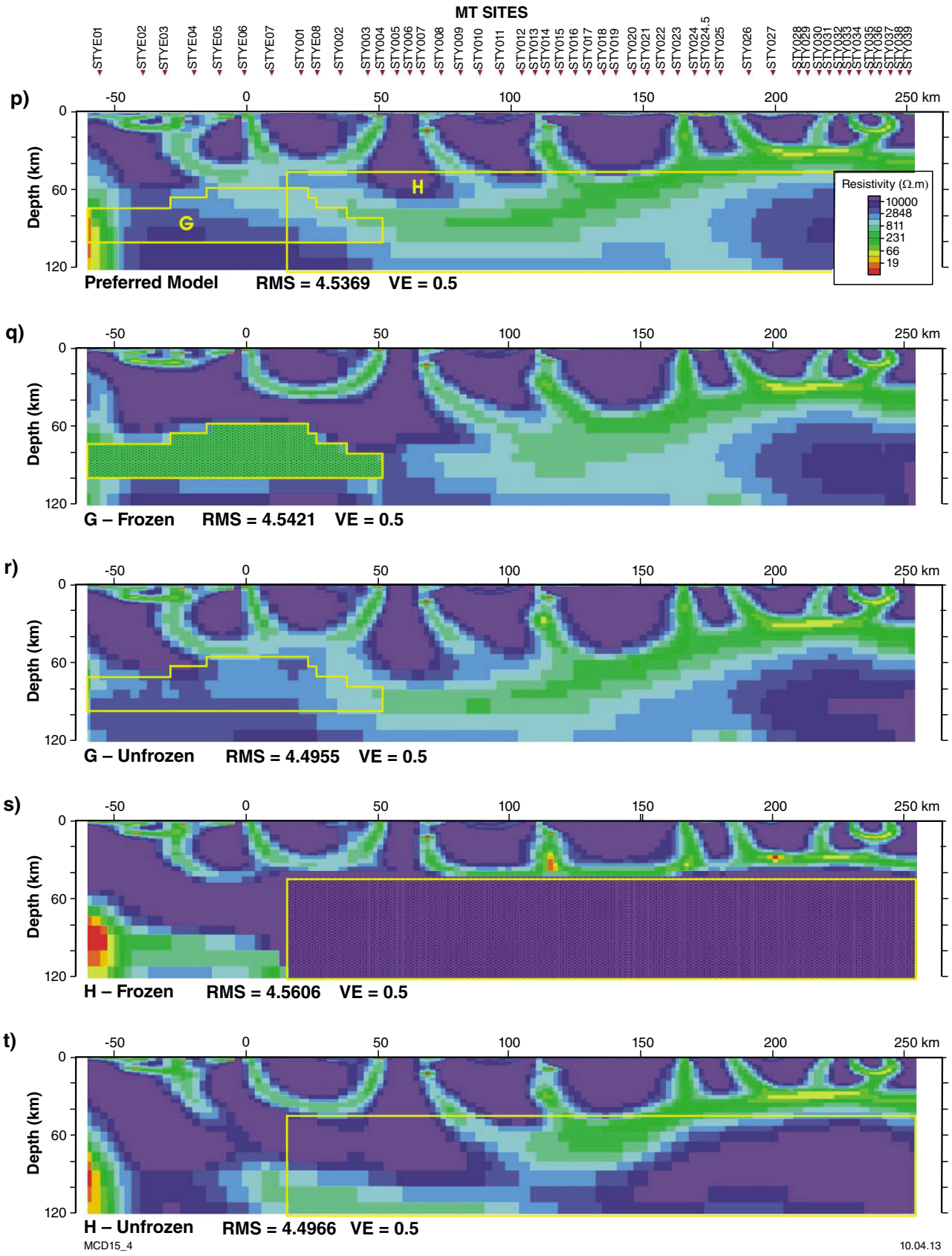

Figure 15. continued

Table 3. RMS misfits derived from feature testing

Feature	*Feature removed*		*Inversion with area frozen*		*Inversion with area unfrozen*	
	RMS misfit	*% change*	*RMS misfit*	*% change*	*RMS misfit*	*% change*
			Dipping conductive zones in crust			
A	4.9642	9.4183	4.5646	0.6105	4.5206	-0.3593
B	4.7129	3.8793	4.6300	2.0521	4.5262	-0.2358
C	4.7030	3.6611	4.5676	0.6767	4.5369	0.0000
D	4.9142	8.3163	4.5501	0.2909	4.5282	-0.1918
E	4.5611	0.5334	4.7300	4.2562	4.5734	0.8045
			Deep crust and mantle layering			
F	6.9625	53.4638	4.6300	2.0521	4.5077	-0.6436
G	5.3649	18.2503	4.5421	0.1146	4.4955	-0.9125
H	9.1193	101.0029	4.5606	0.5224	4.4966	-0.8883

Inversion with the zones frozen achieved reasonable fits for features A, C, and D. For features A and D, conductive zones appeared next to the frozen area. Although the fit for feature C was reasonable, it is not clear how this was achieved, because the resistivity model did not appear to change significantly. The result for feature B showed minor adjustments in the conductive zones either side of it, but the resulting RMS misfit was not as low as in the preferred model. The result for feature E showed a significantly worse RMS misfit.

Inversions with unfrozen areas resulted in conductivity models for all features A–E that were effectively the same as the original, except for C, where there was a change in geometry. Interestingly, in all cases except feature E, re-running the inversion produced the same, or slightly lower, RMS misfit as the preferred model. From the above results, we conclude that the preferred models of dipping conductors are generally reliable, with the possible exception of feature C.

Features F to H are associated with 'layering' in the lower crust and upper mantle. Feature F was chosen to assess the reliability of a conductive zone in the lower crust at the eastern end of the line. Replacing this zone with a resistive region significantly increased the misfit and the frozen feature inversion added conductive material below the area, but could not match the misfit of the preferred model. However, the inversion with feature F unfrozen led to a slightly lower RMS misfit. This was achieved by the appearance of conductive material below the feature. The result is some modification of the dipping upper crustal conductive zones and, as was the case for the frozen result, a shift of the layer of conductive material to greater depth. These results indicate that a conductive layer is required here, but its depth is not well constrained.

Feature G was chosen to assess whether a conductive layer in the upper mantle in the central part of the profile continued to its western end; that is, whether the lateral decrease in resistivity in the preferred model was required. Substituting conductive material caused a significant increase in RMS misfit. Inversion with the area of feature G frozen achieved a reasonable fit, but the geometry of the upper crustal conductors was less geologically convincing. The best fit seen in all the feature tests was achieved by inversion with the region unfrozen, for which higher resistivities returned after inversion. These results indicate that there probably is a lateral change in conductivity in the upper mantle in the area being tested. However, the match to the observed data in this part of the model was generally poor (cf. Fig.14).

Similarly to feature G, feature H was chosen to assess the conductive zone at upper mantle depths, but in the centre of the profile. Replacing this zone with resistive material caused a large increase in RMS misfit. Inversion with the zone frozen produced a slightly poorer fit than the preferred model, with conductive material appearing at the top of the frozen area. Inversion with this zone unfrozen produced a better fit but, although the conductive zone was present, its westward extent was reduced and conductive material appeared at the base of the unfrozen zone. These results indicate that lateral changes in resistivity are required at upper mantle depths but, as was the case for the dipping crustal features, their positions are not well constrained.

Other geophysical data

Dentith et al. (2000) modelled a dataset of long-offset seismic travel times from a traverse which passes about 100 km north of the MT traverse, and found the Moho to be at 35 km at the longitude of the eastern end of the MT traverse. In the same area, Reading et al. (2003) used receiver function analysis to estimate a Moho depth of around 40 km. Reading et al. (2007) compared the seismic velocity – depth profiles for the terranes defined by Cassidy et al. (2006) (Fig. 1), and found that, under the South West Terrane, the Moho is at a depth of 38 km with an overlying velocity gradient. Under the Southern Cross Domain, a sharply defined Moho was located at 38 km. The Moho under the Eastern Goldfields Superterrane was described as sharp and was located at 42 km. Thus, these two types of seismic data suggest the Moho is at about 35–40 km in the study area.

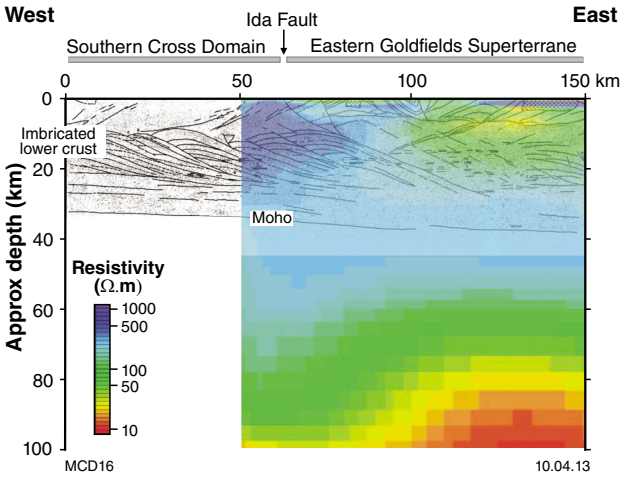

Figure 16. Interpreted seismic reflection profile and MT data across the eastern Southern Cross Domain and western part of Eastern Goldfields Superterrane. See Figure 1 for location. Seismic interpretation from Drummond et al. (2000). MT data are shown as a resistivity cross section derived from an unconstrained inversion by Blewett et al. (2010).

Deep seismic reflection data (line EFG01, Swager et al. 1997; Fig. 1) were recorded to the north and northeast of the Yilgarn MT survey. These comparatively high-resolution data provided information about the geometry of features in the crust and upper mantle, but depth estimates were poorly constrained. Drummond et al. (2000) presented a detailed structural model of a seismic reflection traverse located about 150 km north of the eastern end of the MT traverse (Fig. 1). These data show that the Ida Fault (Fig. 2) is an east-dipping structure extending from surface to the lower crust, and possibly to the base of the crust (Fig. 16). West of the Ida Fault, the middle part of the crust comprises a series of east-dipping reflections that were interpreted as imbricated fault blocks, whereas the lowermost crust has a horizontal reflector fabric. A detachment surface was interpreted between the two zones and the Moho was located at about 35 km. East of the Ida Fault, the lower crust is less structured and the Moho is deeper.

House et al. (1999) described two deep (20 s two-way time) seismic reflection profiles across the Coolgardie and Kambalda Domains in the Eastern Goldfields Superterrane (Fig. 1), to the northeast of the Yilgarn MT survey. They interpreted the domain-bounding faults as listric structures, which have allowed partial imbrication of the domains during regional deformation. The Moho was not directly imaged, but a general decrease in the number of reflections indicates that the crust is about 35 km thick.

Blewett et al. (2010) described MT data coincident with part of the EFG01 seismic line (Fig. 16). The results of an unconstrained inversion show the crust is more conductive to the east of the Ida Fault, although the fault itself does not appear to be associated with a conductivity anomaly. The mantle is conductive below about 60 km depth. Figures 17 and 18 show gravity and magnetic data, respectively, in the vicinity of the south Yilgarn MT traverse. The greenstone belts are clearly distinguished as linear positive gravity anomalies (Fig. 17), due mainly to basaltic units. Sedimentary rocks are associated with gravity lows and ultramafic rocks commonly also have low density due to intense alteration. The other major source of positive gravity anomalies is the extensive easterly trending dyke system in the area. In the magnetic data (Fig. 18), ultramafic rocks are associated with positive linear anomalies. Sedimentary rocks, with the exception of iron formations, and mafic rocks in greenstone belts are generally weakly magnetized. In regions dominated by granites, variations in magnetism reflect their variable magnetite content. The magnetic data clearly show the numerous mafic dykes in the area. These have a range of orientations and may be associated with either positive or negative anomalies, depending on the country rocks and the direction and intensity of their remanent magnetism.

No detailed interpretation of the gravity and magnetic data has been attempted. Rather, the amplitude variation and textural properties of the data have been used to identify regions with similar characteristics. The numerous linears, especially in the magnetic data, represent planar discontinuities, such as repeatedly reactivated shear zones or repeated intrusion of dykes, but distinguishing between these features is difficult because their magnetic responses are the same. The lithospheric boundaries inferred from the MT data (see following section) coincide with changes in the character of the magnetic and gravity data, primarily the frequency and orientation of linears.

Geological implications of the MT data

Figure 19 shows the preferred resistivity cross section derived from the south Yilgarn MT survey data, with various significant conductivity features labelled. Before discussing these features, it is useful to review the current understanding of the causes of electrical conductivity variations at mid-crustal and greater depths, and also the results of other MT surveys in Archean terrains.

Causes of electrical conductivity variations in the deep crust and mantle

Figure 20 summarizes the ranges of conductivities for major crustal layers derived from MT surveys, and from laboratory measurements of various rock types and other materials. The crust is divided into a very resistive upper part and a less resistive lower part, and both are distinct from a somewhat resistive upper mantle.

The resistivity range of crystalline rocks as measured in the laboratory is extremely high (Fig. 20), higher for the most part than the range of observed values for the upper crust, and much higher than for both the lower crust and

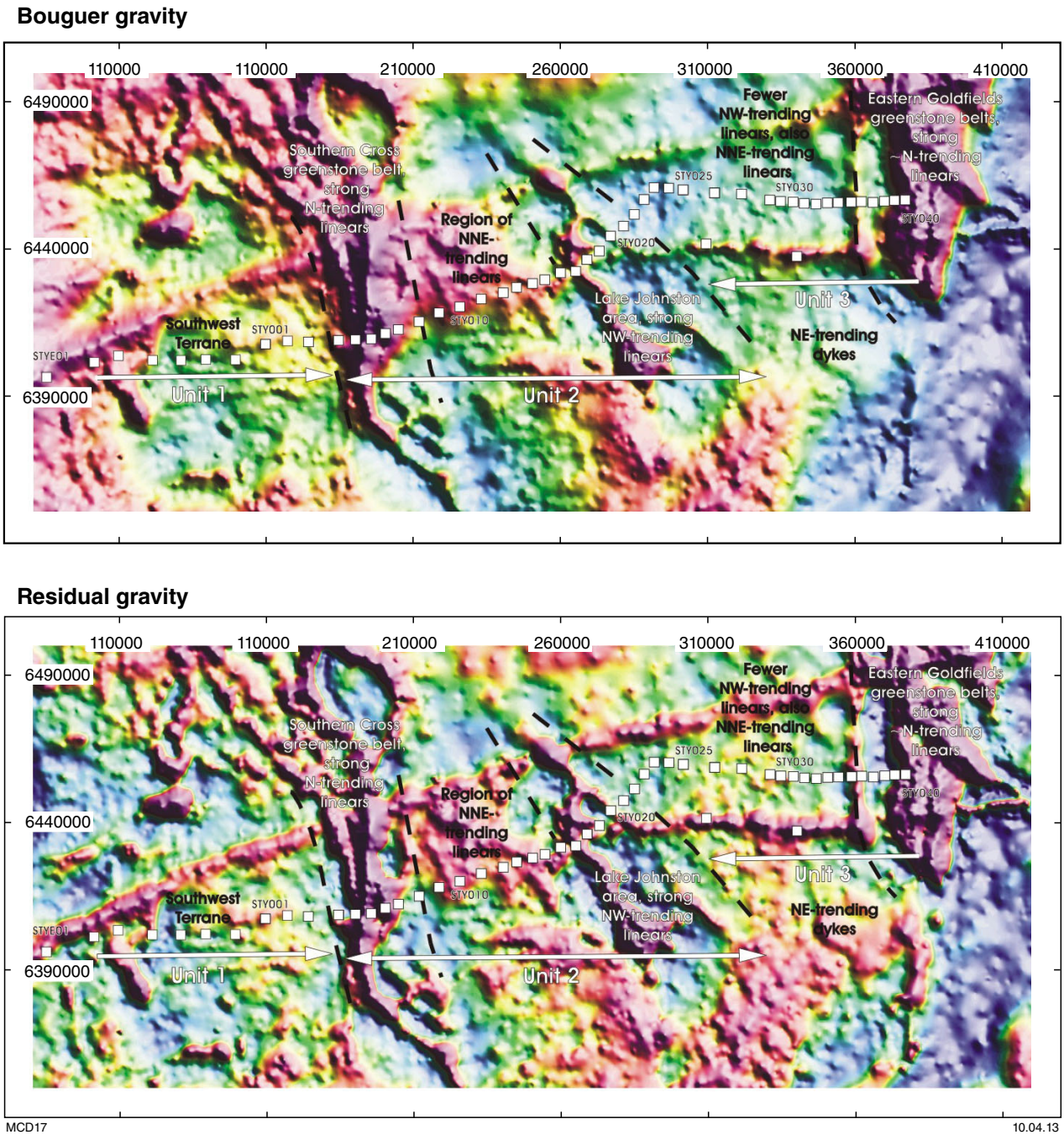

Figure 17. Gravity data from the southern Yilgarn Craton. Data from Geoscience Australia. MT station locations are indicated by squares. Unit subdivisions refer to Figure 19.

continental upper mantle. These relationships have led to a significant body of research on mechanisms that might lower the resistivity of the lower crust and upper mantle rocks in situ, but the cause of the comparatively high conductivity remains unclear (Jones, 1992, 1999). The two most widely supported mechanisms for lowering resistivity in stable continental regions are the presence of fluids (metamorphic brines, partial melts), or conductive mineral species (graphite, sulfides). However, studies of these mechanisms have been hindered by the need to recreate extreme conditions of temperature and pressure in the laboratory and the difficulty of accounting for the effects of time on a geological scale. One explanation attributes the lower resistivities to the effect of conductive graphite films on grain boundaries. An explanation that reduced resistivity is due to the presence of saline fluids is weakened by the argument that free water is unlikely to be present in the deep crust. The likelihood of very low porosity and permeability in the lower crust and mantle also conflicts with a fluid-related increase in conductivity.

Regardless of the type of conducting material, it is important to recognize that interconnectivity of conducting elements is a key control on overall conductivity of a material. If

Total magnetic intensity

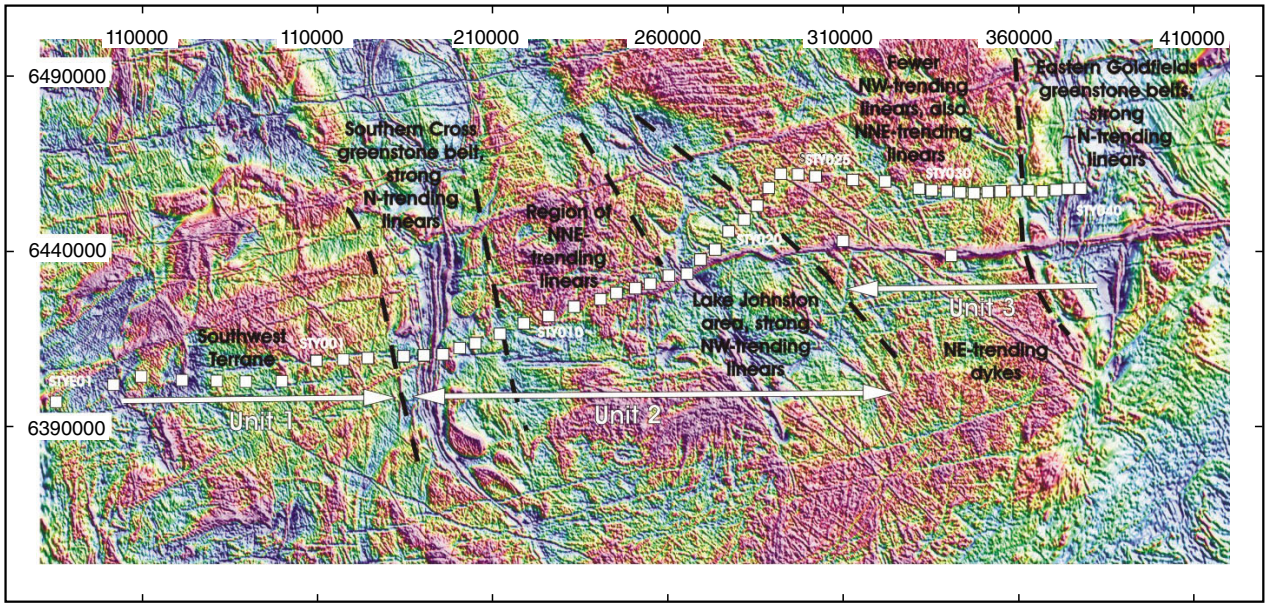

1st vertical derivative of total magnetic intensity

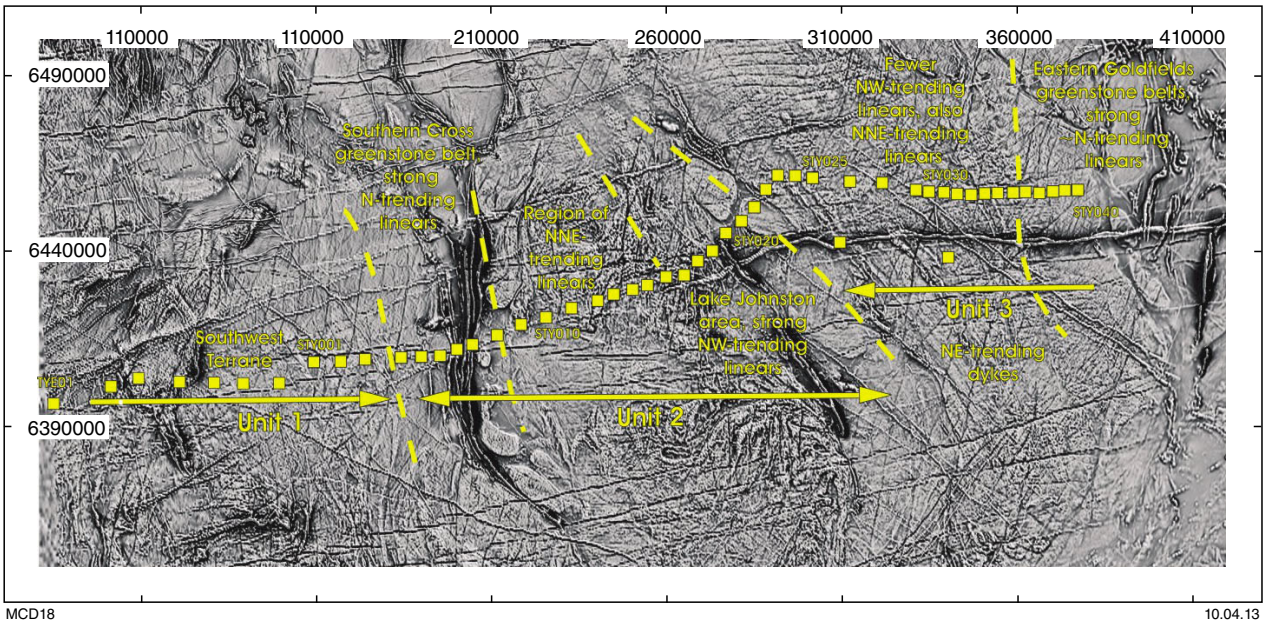

Figure 18. Total magnetic intensity (TMI) data, and 1st vertical derivative of TMI, from the southern Yilgarn Craton. Data from Geoscience Australia. MT station locations are indicated by squares. Unit subdivisions refer to Figure 19.

there is interconnectivity, only small amounts of conductive components are required. MT survey data are a response to conductance, the product of conductivity and thickness, so apparently broad regions of enhanced conductivity may be due to quite thin zones of high conductivity. It is also worth noting that continuous networks of conductive material (of whatever type) over very large areas of enhanced conductivity are difficult to explain, as is maintaining their continuity over geological time scales.

At mantle depths, electrical characteristics reflect the properties of olivine. Similar to crustal responses, a major difficulty in understanding electrical responses from the mantle is that laboratory measurements of the resistivity of olivine suggest that mantle resistivity should be much higher than that derived from MT measurements. The resistivity of dry olivine decreases with increasing temperature, by approximately one order of magnitude for every 200–300°C (Constable, 2006). Nevertheless, models based on these data appear to underestimate the electrical conductivity of the mantle. The effect of pressure on conductivity is small, whereas the effect of oxygen fugacity on conductivity is more than half an order of magnitude higher than that of pressure at high

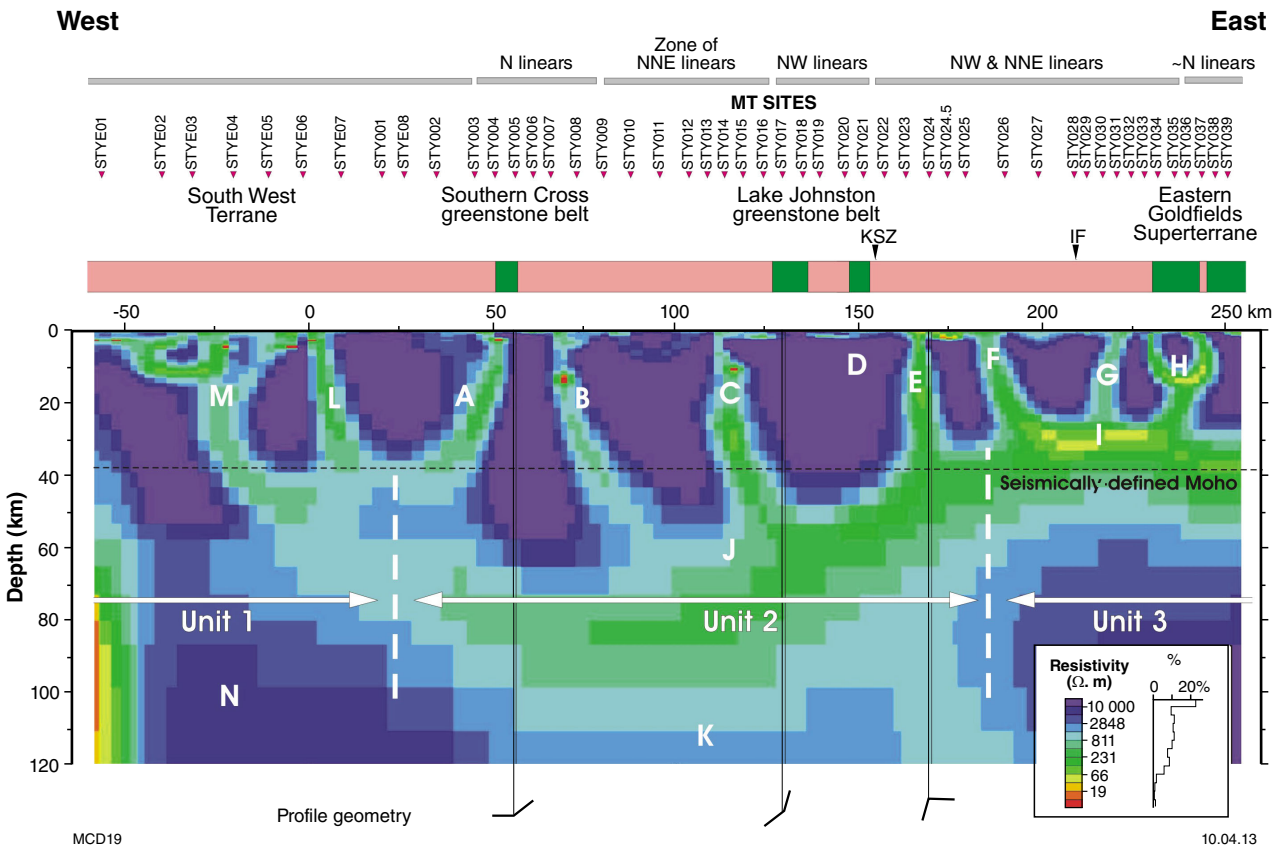

Figure 19. Resistivity cross section derived from 2D inverse modelling of MT data shown in Figure 12. KSZ – Koolyanobbing Shear Zone, IF – Ida Fault. Annotations A to N are geoelectrical features discussed in text.

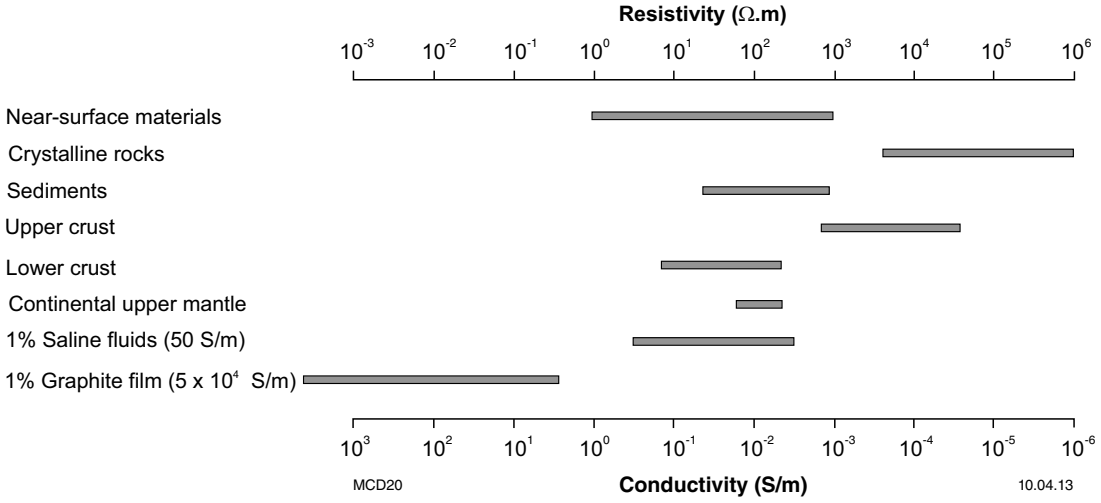

Figure 20. Resistivity ranges of selected geological entities and other materials. Redrawn from Jones (1999) with additions.

temperatures (Constable, 2006; Jones et al., 2009 and references therein). Other factors that have been suggested as affecting (decreasing) resistivity include the presence of dissolved hydrogen, carbon on grain boundaries, or partial melt. The grain size of mantle olivine may also be a factor. Changes in grain size appear to be capable of causing order-of-magnitude changes in electrical properties, with an inverse relationship between conductivity of olivine and its grain size (Ten Grotenhius et al., 2004).

Electrical conductivity in Canadian Archean terrains

A considerable number of MT surveys have been undertaken on the Canadian Shield. These data confirm that the lower crust in such areas is commonly conductive, but this is by no means always the case (e.g. the Slave and Rae Cratons; Jones et al., 2002); low and high conductivity can be observed in adjacent areas of the lower crust. Where there is no conductive lower crust, it may be possible to map the depth to the 'electrical' Moho. This cannot be achieved where the crust is conductive because of the limited ability of electromagnetic methods to map the depth to the base of a conductive zone.

Many of the MT surveys on the Canadian Shield crossed major crustal structures, such as boundaries between Archean blocks and adjacent Proterozoic terranes, or structures separating geologically distinct domains within the Archean blocks. Such structures have been observed to correlate with both conductive and resistive features in the MT data. Another possibility is that major geological structures or boundaries manifest in MT data not as specific conductivity feature, but as the juxtaposition of lithosphere with different vertical variations in conductivity. A good example of a structure that coincides with a resistive zone is provided by the Great Slave Lake Shear Zone (Wu et al., 2002). This very large structure separates Proterozoic terranes in northwestern Canada and was found by Wu et al. (2002) to coincide with a subvertical resistive zone (resistivity ~ 10 000 Ω.m, width ~ 20 km). The source of the high resistivities is thought to be mylonites formed from a granitic protolith. Stockwork quartz veins may also contribute to the high resistivity.

An excellent example of a conductive fault zone is the West Bay – Indin Fault of the Slave Craton. Spratt et al. (2009) described an MT survey extending from the Slave Craton across the adjacent Bear Province, which were brought together during the Paleoproterozoic Wopmay Orogeny (Fig. 21). They interpreted the Wopmay Fault Zone as the surface expression of the suture between Proterozoic and Archean blocks. Geological and isotopic evidence suggest the fault marks the western limit of Archean crust. As discussed in the next section, the MT results from the Slave Craton resemble those from the south Yilgarn MT survey. An electrical Moho interpreted by Spratt et al. (2009) at a depth of 32–35 km is consistent with seismic studies to the south of the MT traverse (reference). The crust is generally resistive, but the underlying mantle less so. Within the mantle, and extending from the Moho to more than 150 km depth, there is a distinct change in resistivity between locations 50 and 100 km along the profile (Fig. 21). This was interpreted as marking the western edge of the resistive cratonic root of the Slave Province. Note that it lies well to the west of the Wopmay Fault Zone. The cause of the high conductivity is unconstrained, although it may be an olivine grain-size effect associated with shear zones in the mantle.

The Slave Craton has two zones of high conductivity within the crust in the area studied by Spratt et al. (2009). They interpreted the feature at around 215 km on the profile as a body of interconnected sulfides, possibly related to sedimentary rocks. The second high-conductivity feature reaches the surface at around 240 km on the profile and dips to the east at about 50°, extending through the entire crust. This features correlates with the West Bay – Indin Fault Zone and adjacent parallel structures, and the source of the enhanced conductivity was similarly interpreted to be sulfide mineralization within the fault zone.

In addition to defining both the electrical structure of Archean lithosphere and major fault structures, a significant result from the Canadian work is that changes in electrical properties in the deep crust and mantle are commonly laterally offset from major structures and suture zones mapped at the surface (Jones et al., 2002). This may be a response to the dip of the structures, or may reflect delaminating tectonic processes, whereby large 'wedge-like' pieces of crust and mantle interleave in the suture zone (Spratt et al., 2009).

Electrical conductivity in the southern Yilgarn Craton

The upper crust in the area of the south Yilgarn MT survey is mostly highly resistive (~10 000 Ω.m or greater; Fig. 19). This is typical of the upper crust and consistent with laboratory measurements of crystalline rocks (Fig. 20). Around 20% of the preferred resistivity model exhibits such high resistivities (Fig. 19 inset) and, in some areas, resistivity is considerably greater than 10 000 Ω.m (the need to effectively display parts of the model with lower resistivities means these variations are not obvious in Figure 19). The highly resistive zones are separated by more conductive regions, mostly narrow and dipping either east or west. Based on comparison with equivalent data from the Canadian Shield (Fig. 21), these zones are interpreted as major fault or shear zones. Some of these (e.g. features B and E of Fig. 19) appear to extend through the entire crust, and others reach at least mid-crustal levels (e.g. features F and G). These depths are consistent with the depth extent of structures interpreted from seismic reflection data (Fig. 16).

There is evidence for major structures on both sides of the Southern Cross greenstone belt (features A and B, but note our earlier discussion regarding the reliability of feature B), and there are equivalent major potential field linears (Figs 17 and 18). A conductive zone in the upper crust immediately west of the Lake Johnston greenstone belt (feature C) is within a zone of intense north-northeasterly trending magnetic linears (Fig. 18). This feature is not shown on geological maps and appears to be a new structure revealed by the MT survey data.

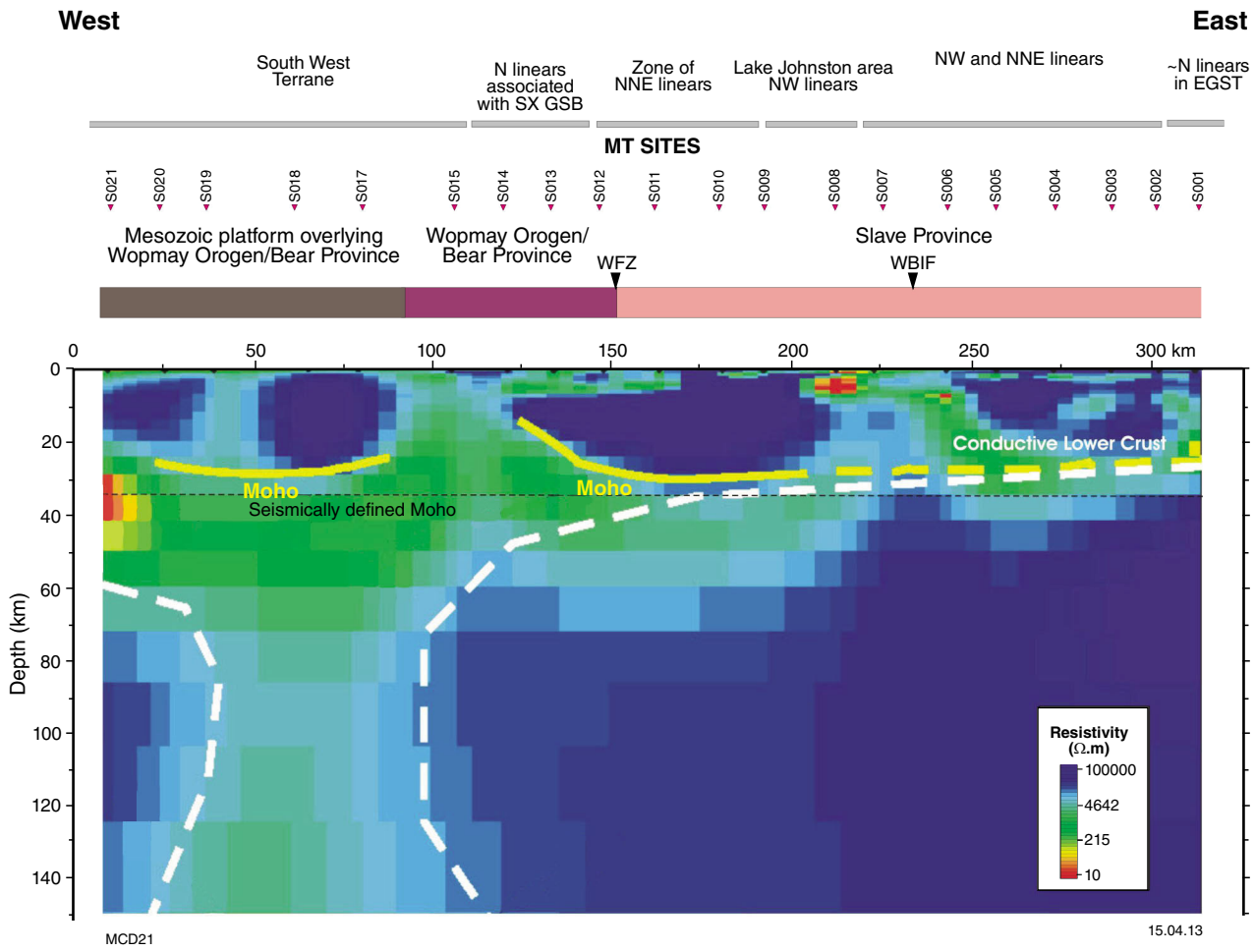

Figure 21. Electrical resistivity cross section across the Slave Province and adjacent Proterozoic orogen in northern Canada. For comparison, major structures along the south Yilgarn MT traverse are also shown. WFZ – Wopmay Fault Zone, WBIF – West Bay – Indin Fault, SX GSB – Southern Cross greenstone belt, EGST – Eastern Goldfields Superterrane. Yellow lines mark the crust–mantle boundary and white dashed lines delineate cratonic roots beneath the Slave and Bear Provinces. Redrawn from Spratt et al. (2009).

The Koolyanobbing Shear Zone, although a major structure in terms of surface geology and magnetic and gravity data, does not seem to coincide with either of the nearby geoelectrical features D or E. Notably, Libby et al. (1991) described the Koolyanobbing Shear Zone as a 6 to 15 km wide zone of mylonitic rocks derived from monzogranite to tonalite parent rocks. This is consistent with a weak conductivity anomaly, and is comparable to the resistive character of the Great Slave Lake Shear Zone. Alternatively, the Koolyanobbing Shear Zone may be further to the east than shown on current geological maps and coincide with feature E. Movement on the Koolyanobbing Shear Zone is thought to be predominantly transcurrent (Angerer and Hagemann, 2010), which would be consistent with the steep dip of feature E (Fig. 19).

In the vicinity of the eastern end of the south Yilgarn MT traverse, there are numerous important structures defining terrane and domain boundaries within the Eastern Goldfields Superterrane (Figs 1 and 2). Feature G approximately coincides with the location of one of these, the Ida Fault as shown on Figure 2. However, the position of the fault is not geologically well constrained and there are no magnetic or gravity features (Figs 17 and 18) that coincide with the Ida Fault as shown in Figure 2. Also, no MT response was associated with the mapped trace of the Ida Fault farther north (Fig. 16). Feature H appears to be related to major faults at the western margin of the greenstone belts of the Eastern Goldfields Superterrane. At the western end of the MT traverse, features A, L, and M may be associated with a series of structures at, or near, the eastern boundary of the South West Terrane.

The most significant variations in electric resistivity are at stations STY023–025. There are two zones of lower resistivity (E and F) along this section of the traverse; these are interpreted here as major fault structures. Because of the resistivity variations at subcrustal depths (discussed below), these features are together considered to be the mostly likely candidate for a major suture or paleocratonic boundary in the region. Interestingly, these geoelectric features are in an area where both gravity and magnetic data are relatively homogeneous, with the exception of a pair of northwest-trending dykes evident in

the magnetic data (Fig. 18), which do not appear to have equivalents elsewhere in the study area.

Conductivity variations in the lower crust and upper mantle are of particular interest, although, as noted above, the MT data may not constrain their depth extent very well. To the east, feature I is consistent with a conductive lower crust and the depth to its base is in reasonable agreement with the seismically defined Moho. The small depth discrepancy can be explained by the fundamental inability of the MT method to resolve the depth to the base of conductors. The westward limit of the conductive lower crust coincides with features E and F in the lower crust. Farther west, there is no evidence for conductive lower crust; instead, the upper mantle is more conductive (feature J). The geometry of the zone of more conductive mantle represented by feature J is intriguing. It appears to deepen to the west before shallowing and passing laterally into a zone of more resistive mantle (feature N), although the position of this transition is not well constrained. The transition broadly coincides with conductive zones A and L in the crust, but it is unclear if these two types of features are related.

Feature K is a more conductive zone compared with mantle to the east and the west at depths of around 100 km. However, it is questionable whether feature K is real, as it is close to the maximum depth of penetration of useful MT data. It is an attractive option to link this feature to alteration of material in the deep mantle, but the crust and mantle are quite resistive overall, so the data may be sensing the Southern Ocean some 180 km south of the traverse.

Based on the above, it is proposed that the MT survey has defined two, or possibly three, major 'blocks' of lithosphere: Units 1, 2, and 3 (Figs 17, 18, and 19). The distinction between units 2 and 3 is based on their different geoelectrical properties in the lower crust and upper mantle. Placing a major lithospheric boundary between units 2 and 3 is consistent with isotopic ages from the Southern Cross and Lake Johnston greenstone belts, which do not contain rocks with the younger ages as found in the greenstones of the Eastern Goldfields.

The distinction between units 1 and 2 is made with less confidence. The extension of the MT survey to the west (campaign 3) was intended to clarify this. However, mantle conductivity structure west of station STY001 is quite complex and may not be well constrained. Also, the MT data from this part of the traverse must be treated with caution because the fit of the preferred model to observed data at stations STYE04–06 was poor. The preferred interpretation is that there is an eastward decrease of mantle conductivity between units 1 and 2, but, unlike the other end of the traverse, there is no evidence for a conductive lower crust. This interpretation of a change in lithospheric character is, however, consistent with the geological distinction between the South West Terrane and the greenstone-hosting terranes to the east. It is also consistent with the interpretation by Reading et al. (2007) of seismic receiver function data, which define differences in vertical crustal velocity profiles in the two regions. The location of the boundary between units 1 and 2 is poorly defined. It is tempting to extend the apparently east-dipping features in the crust into the mantle and propose a tectonic feature of similar geometry in the mantle. In this case, the projection to the surface of the change coincides with features L or M, or both. A steeply west-dipping boundary coincident with feature A cannot be ruled out, however.

The boundary between units 2 and 3 may mark the location, at least in the deep crust, of the western extent of the Eastern Goldfields Superterrane. This inferred boundary coincides with the Ida Fault to the north of the MT survey area, where seismic reflection data (Fig. 16) suggest a coincident change in the nature of the lower crust across the fault from the Southern Cross Domain lower crust, with imbricated fault blocks, to the Eastern Goldfields Superterrane, characterized by flat reflectors. If the boundary between units 2 and 3 represents the Ida Fault, then the position of the Ida Fault shown on Figure 2 is too far to the east, or the boundary at the surface does not coincide with the boundary in the deep crust. Either of these is possible, given that, as previously discussed, the location of the Ida Fault is otherwise poorly constrained in the study area. Furthermore, because of a lack of isotopic data in the study area (due to the lack of suitable outcrop), the position of the change in isotopic character from the Eastern Goldfields terranes to those farther west is poorly constrained.

The boundary between units 1 and 2 is most likely related to the boundary between the South West Terrane and the Youanmi Terrane. The surface geological boundary between these terranes is close to feature A, but this boundary (or at least the large faults associated with it) has a distinct 'jog' and, south of the MT traverse, is located farther to the west (Figs 1 and 2). Thus, feature M or L might also be associated with the boundary. Another possible scenario is that features L and M are associated with terrane or domain boundaries within the South West Terrane, which is poorly understood and could well be a composite feature, and Wilde et al. (1996) suggested the presence of subterranes or domains. The poorly defined eastern margin of their Lake Grace terrane is possibly responsible for feature L.

Referring to the presence or absence of a conductive lower crust, Jones and Garcia (2006) stated that 'the locations of resistive crust are all Archean in age, and likely Mesoarchean or earlier' and 'continental crust of ages younger than Mesoarchean predominantly display a conducting lower crust'. The implication from this for the south Yilgarn MT traverse is that unit 2 is Mesoarchean (3.2 – 2.8 Ga) and unit 3 is Neoarchean (2.8 – 2.5 Ga). These ages would be consistent with isotopic ages from the greenstone belts at the surface. However, it is common for the positions of mantle terrane boundaries to not coincide with surface terrane boundaries (Spratt et al., 2009). Perhaps the most significant tectonic implication of the south Yilgarn MT data lies in the lateral changes of geoelectrical properties in the lower crust and mantle. Although marked changes in the near-surface geology of the Yilgarn Craton are well known, the recognition of lateral changes at depth is comparatively recent (e.g. the isotopic data of Cassidy et al., 2006). The MT results

described here show that regions of mantle with different geoelectrical properties, and by implication geological history, can be defined.

The observation that changes of features at the surface do not necessarily coincide with those at depth suggests that major detachment surfaces may exist at depth and that some of the regions between the detachments may be allochthonous, or at least parautochthonous. Furthermore, given the emphasis in recent regional-scale exploration targeting models on the prospectivity of paleocraton margins (Begg et al., 2010; McCuaig et al., 2010), this is an important result that, together with the capability of MT data for mapping deep-penetrating structures (also important features in regional targeting models), demonstrates the usefulness of MT surveys of the type described here.

Conclusions

The magnetotelluric survey described here has allowed electrical conductivity variations in the crust and upper mantle to be determined along a 300-km-long traverse across the southern Yilgarn Craton. Based on the electrical resistivity variations observed, a three-fold division of the crust and upper mantle is inferred, which is consistent with surface geological mapping of terrane boundaries. A change in electrical properties at the western end of the MT traverse coincides with the boundary between the South West Terrane and the Youanmi Terrane (Southern Cross Domain). However, the MT data indicate that the boundary between the Southern Cross Domain and the Eastern Goldfields Superterrane may be 50 km farther west than previously thought. This might be a function of deep crustal boundaries being laterally offset from major surface structures, as has been observed in the Canadian Shield.

Collecting MT data is comparatively quick and cheap. The data from the south Yilgarn MT survey demonstrate that such data can be used to map large structures and the boundaries between major crustal blocks in the deep crust and upper mantle. These features are important indicators of mineral prospectivity at the regional scale.

Acknowledgements

The south Yilgarn MT survey was funded by the Exploration Incentive Scheme of the Western Australian Government. We acknowledge very useful reviews of this work by Ian Ferguson and Graham Begg. Ian Tyler is also thanked for his support and interest in MT surveys in Western Australia.

References

Ahmat, AL 1986, Metamorphic patterns in the greenstone belts of the Southern Cross Province, Western Australia: Geological Survey of Western Australia, Professional papers for 1984, Report 19, p. 1–21.

Allibone, AH, Windh, J, Etheridge, MA, Burton, D, Anderson, G, Edwards, PW, Miller, A, Graves, C, Fanning, CM and Wysoczanski, R 1998, Timing relationships and structural controls on the location of Au–Cu mineralisation at the Boddington gold mine: Economic Geology, v. 93, p. 245–270.

Angerer, T and Hagemann, SC 2010, The BIF-hosted high-grade iron ore deposits in the Archean Koolyanobbing greenstone belt, Western Australia: structural control on synorogenic- and weathering-related magnetite-, hematite-, and goethite-rich iron ore: Economic Geology, v. 105, p. 917–945.

Barley, ME and Groves, DI 1987, Hydrothermal alteration of Archaean supracrustal sequences in the central Norseman–Wiluna Belt, Western Australia: a brief review, *in* Recent Advances in Understanding Precambrian Gold Deposits *edited by* SE Ho and DI Groves: Geology Department and University Extension, The University of Western Australia, Publication 11, p. 51–66.

Barley, ME, Krapež, B, Groves, DI and Kerrich, R 1998, The Late Archean bonanza: metallogenic and environmental consequences of the interactions between mantle plumes, lithospheric tectonics and the global cyclicity: Precambrian Research, v. 91, p. 65–90.

Begg, GC, Hronsky, JMA, Arndt, NT, Griffin, WL, O'Reilly, S and Hayward, N 2010, Lithospheric, cratonic, and geodynamic setting of Ni–Cu–PGE sulfide deposits: Economic Geology, v. 105, p. 1057–1070.

Blewett, RS, Henson, PA, Roy, IG, Champion, DC and Cassidy, KF 2010, Scale-integrated architecture of a world-class gold system: The Archaean eastern Yilgarn craton: Precambrian Research, v. 183, p 230–250.

Buck, PS, Vallance, SA, Perring, CS, Hill, RE and Barnes, SJ 1998, Maggie Hays nickel deposit, *in* Geology of Australian and Papua New Guinean Mineral Deposits *edited by* DA Berkman and DH Mackenzie: The Australasian Institute of Mining and Metallurgy, Melbourne, Australia, p. 357–364.

Caldwell, TG, Bibby, HM and Brown, C 2004, The magnetotelluric phase tensor: Geophysical Journal International, v. 158, p. 457–469.

Cassidy, KF and Champion, DC 2004, Crustal evolution of the Yilgarn Craton from Nd isotopes and granite geochronology: implications for metallogeny, *in* Predictive Mineral Discovery Under Cover *edited by* JR Muhling, RJ Goldfarb, NM Vielreicher, FP Bierlein, E Stumpfl, DI Groves, S Kenworthy and CM Knox-Robinson: Centre for Global Metallogeny, The University of Western Australia; SEG 2004, Perth, Western Australia, 27 September 2004; Extended Abstracts, p. 317–320.

Cassidy, KF, Champion, DC, Krapež, B, Barley, ME, Brown, SJA, Blewett, RS, Groenewald, PB and Tyler, IM 2006, A revised geological framework for the Yilgarn Craton, Western Australia: Geological Survey of Western Australia, Record 2006/8, 8p.

Cassidy, KF, Champion, DC, McNaughton, N, Fletcher, IR, Whitaker, AJ, Bastrakova, IV and Budd, A 2002, The characterisation and metallogenic significance of Archaean granitoids of the Yilgarn Craton, Western Australia: Minerals and Energy Research Institute of Western Australia (MERIWA), Project no. M281/AMIRA Project no. 482 (unpublished report no. 222).

Champion, DC and Cassidy, KF 2007, An overview of the Yilgarn and its crustal evolution, *in* Proceedings of Kalgoorlie 2007 Conference *edited by* FP Bierlein and CM Knox-Robinson: Geoscience Australia; Kalgoorlie, Western Australia, 25 September 2007; Record 2007/14, p. 8–13.

Chen, SF, Riganti, A, Wyche, S, Greenfield, JE and Nelson, DR 2003, Lithostratigraphy and tectonic evolution of contrasting greenstone successions in the central Yilgarn Craton, Western Australia: Precambrian Research, v. 127, p. 249–266.

Chin, RJ, Hickman, AH and Thom, R (compilers) 1984, Hyden, Western Australia (Sheet SI 50-4): Geological Survey of Western Australia, 1:250 000 Geological Series Explanatory Notes, 21p.

Condie, KC 1997, Contrasting sources for upper and lower continental crust: the greenstone connection: Journal of Geology, v. 105, p. 729–736.

Constable, SC 2006, SEO3: A new model of olivine electrical conductivity: Geophysical Journal International, v. 166, p. 435–437.

Dentith, MC, Dent, VF and Drummond, BJ 2000, Deep crustal structure in the southwestern Yilgarn Craton, Western Australia: Tectonophysics, v. 325, p. 227–255.

Doepel, JJG (compiler) 1973, Norseman, Western Australia: Geological Survey of Western Australia, 1:250 000 Geological Series Explanatory Notes, 40p.

Drummond, BJ, Goleby, BR and Swager, CP 2000, Crustal signature of Late Archean tectonic episodes in the Yilgarn craton, Western Australia: evidence from deep seismic sounding: Tectonophysics, v. 329, p. 193–221.

Fiorentini, ML, Barnes, SJ, Maier, WD, Burnham, OM and Heggie, G 2011, Global variability in the platinum-group element contents of komatiites: Journal of Petrology, v. 52, no. 1, p. 83–112.

Fletcher, IR and McNaughton, NJ 2002, Granitoid geochronology: SHRIMP zircon and titanite data, *in* The Characterisation and Metallogenic Significance of Archaean Granitoids of the Yilgarn Craton, Western Australia *edited by* KF Cassidy, DC Champion, NJ McNaughton, IR Fletcher, AJ Whitaker, IV Bastrakova and A Budd: Minerals and Energy Research Institute of Western Australia (MERIWA), Project no. M281/AMIRA Project no. 482 (unpublished report no. 222), p. 1–156.

Gamble, TD, Goubau, WM and Clarke, J 1979, Magnetotellurics with a remote reference: Geophysics, v. 44, p. 53–68.

Gee, RD 1981, Southern Cross, WA Sheet SH50-16: Geological Survey of Western Australia, 1:250 000 Geological Series.

GEOSYSTEM SRL 2008, WinGLink® user's guide, release 2.20.02.01: GEOSYSTEM SRL, Milan, Italy, 473p.

Goscombe, B, Blewett, RS, Czarnota, K, Groenewald, PB and Maas, R 2009, Metamorphic evolution and integrated terrane analysis of the eastern Yilgarn Craton: Rationale, methods, outcomes and interpretation: Geoscience Australia, Record 2009/23, 270p.

Groves, DI and Barley, ME 1994, Mineralization in Western Australia, in Archean Crustal Evolution: Elsevier, Amsterdam, The Netherlands, p. 461–503.

Heggie, G 2010, The scale of PGE variation in mineralised komatiites from the Yilgarn Craton of Western Australia: The University of Western Australia, Perth, Western Australia, PhD thesis (unpublished), 257p.

Hill, RE and Campbell, IH 1993, Age of granite emplacement in the Norseman region of Western Australia: Australian Journal of Earth Sciences, v. 40, p. 559–574.

Hill, RE, Campbell, IH and Compston, W 1989, Age and origin of granitic rocks of the Kalgoorlie–Norseman region, Western Australia: implications for the origin of Archaean crust: Geochimica et Cosmochimica Acta, v. 53, p. 1259–1275.

Hill, RE, Chappell, BW and Campbell, IH 1992, Late Archean granites of the southeastern Yilgarn Block, Western Australia: age, geochemistry, and origin: Royal Society of Edinburgh, Transactions: Earth Sciences, v. 83, p. 211–226.

Hoatson, DM, Jaireth, S and Jaques, AL 2011, Nickel sulfide deposits in Australia: characteristics, resources and potential: Ore Geology Review, v. 29, p. 177–241.

House, M, Dentith, MC, Trench, A, Groves, DI and Miller, D 1999, Structure of the highly mineralised late-Archaean granitoid–greenstone terrain and the underlying crust in the Kambalda–Widgiemooltha area, Western Australia, from the integration of geophysical datasets: Exploration Geophysics, v. 30, p. 50–67.

Joly, A, Miller, J and McCuaig, TC 2010, Archean polyphase deformation in the Lake Johnston Greenstone Belt area: Implications for the understanding of ore systems of the Yilgarn Craton: Precambrian Research, v. 177, p. 181–198.

Jones, AG 1992, Electrical conductivity of the continental lower crust, *in* Continental lower crust *edited by* DM Fountain, R Arcu Arculus and RW Kay: Elsevier, Amsterdam, The Netherlands, Developments in geotectonics 23, p. 81–144.

Jones, AG 1999, Imaging the continental upper mantle using electromagnetic methods: Lithos, v. 48, p. 57–80.

Jones, AG, Evans, RL and Eaton, DW 2009, Velocity–conductivity relationships for mantle mineral assemblages in Archean cratonic lithosphere based on a review of laboratory data and Hashin–Shtrikman extremal bounds: Lithos, v. 109, p. 131–143.

Jones, AG and Garcia, X 2006, Electrical resistivity structure in the Yellowknife River fault zone and surrounding region, *in* Gold in the Yellowknife Greenstone Belt, Northwest Territories: results of the EXTECH III Multidisciplinary Research Project *edited by* CD Anglin, H Falck, DF Wright and EJ Ambrose: Geological Association of Canada, Mineral Deposits Division, Special Publication 3, p. 126–141.

Jones, AG and Jödicke, H 1984, Magnetotelluric transfer function estimation improvement by a coherence based rejection technique (EM1.5), *in* Abstract Volume: 54th Society of Exploration Geophysics Annual General Meeting, Atlanta, Georgia, USA, SEG Extended Abstracts v. 3, p. 51–55.

Jones, AG, Snyder, D, Hammer, S, Asudeh, I and White, D 2002, Magnetotelluric and teleseismic study across the Snowbird tectonic zone, Canadian shield: a Neoarchean mantle suture: Geophysical Research Letters, v. 29, p. 10-1 – 10-4, doi:10.1029/2002GL015359.

Kositcin, N, Brown, SJA, Barley, ME, Krapež, B, Cassidy, KF and Champion, DC 2008, SHRIMP U–Pb zircon age constraints on the Late Archaean tectonostratigraphic architecture of the Eastern Goldfields Superterrane, Yilgarn Craton, Western Australia: Precambrian Research, v. 161, p. 5–33.

Krapež, B, Brown, SJA, Hand, J, Barley, ME and Cas, RAF 2000, Age constraints of recycled crustal and supracrustal sources of Archaean metasedimentary sequences, Eastern Goldfields Province, Western Australia: evidence from SHRIMP zircon dating: Tectonophysics, v. 332, p. 89–133.

Libby, J, Groves, DI and Vearncombe, JR 1991, The nature and tectonic significance of the crustal-scale Koolyanobbing shear zone, Yilgarn Craton, Western Australia: Australian Journal of Earth Sciences, v. 38, p. 229–245.

Mazzucchelli, RH and Robins, TW 1973, Geochemical exploration for base and precious metal sulphides associated with the Jimberlana dyke, Western Australia: Journal of Geochemical Exploration, v. 2, no. 4, p. 383–392.

McCuaig, TC, Beresford, B and Hronsky, J 2010. Translating the mineral systems approach into an effective exploration targeting system: Ore Geology Reviews, v. 38, p. 128–138.

McCuaig, TC and Kerrich, R 1998, P–T–t-deformation-characteristics of lode gold deposits: evidence from alteration systematics: Ore Geology Review, v. 120, p. 381–453.

McGoldrick, PJ 1993, Norseman, WA Sheet 3233: Geological Survey of Western Australia, 1:100 000 Geological Series.

Mole, DR, Fiorentini, ML, Thebaud, N, McCuaig, TC, Cassidy, KF, Barnes, SJ, Belousova, EA, Mudrovska, I and Doublier, MP 2010, Lithospheric controls on the localization of komatiite-hosted nickel-sulfide deposits: evolving early Earth, *in* Fifth International Archean Symposium Abstracts *edited by* IM Tyler and CM Knox-Robinson: Geological Survey of Western Australia, Record 2010/8, p. 101.

Mueller, AG and McNaughton, NJ 2000, U–Pb ages constraining batholith emplacement, contact metamorphism, and the formation of gold and W–Mo skarns in the Southern Cross area, Yilgarn Craton, Western Australia: Economic Geology, v. 95, p. 1231–1258.

Nelson, DR 1995, Compilation of SHRIMP U–Pb zircon geochronology data, 1994: Geological Survey of Western Australia, Record 1995/3, 244p.

Nelson, DR 1997, Compilation of SHRIMP U–Pb zircon geochronology data, 1996: Geological Survey of Western Australia, Record 1997/2, 189p.

Nemchin, AA and Pidgeon, RT 1997, Evolution of the Darling Range Batholith, Yilgarn Craton, Western Australia: a SHRIMP zircon study: Journal of Petrology, v. 38, p. 625–649.

Nemchin, AA, Pidgeon, RT and Wilde, SA 1994, Timing of Late Archaean granulite facies metamorphism in the southwestern Yilgarn Craton of Western Australia: evidence from U–Pb of zircons from mafic granulites: Precambrian Research, v. 68, p. 307–321.

Pawley, M, Romano, SS, Hall, CE, Wyche, S and Wingate, MTD 2009, The Yamarna Shear Zone: a new terrane boundary in the northeastern Yilgarn Craton?, *in* Geological Survey of Western Australia Annual Review 2007–08: Geological Survey of Western Australia, Perth, Western Australia, p. 27–33.

Pellerin, L., Schmidt, J.M., and Hoversten, G.M., 2003, Two-dimensional inverse and three-dimensional forward modelling of MT data to evaluate the mineral potential of the Amphitheater Mountains, Alaska, USA, *in* Proceedings of the 3rd International Symposium in Three-dimensional Electromagnetics (3DEM-3), Adelaide, South Australia.

Perring, CS, Barnes, SJ and Hill, RET 1996, Geochemistry of komatiites from Forrestania, Southern Cross Province, Western Australia: evidence for crustal contamination: Lithos, v. 37, p. 181–197.

Pidgeon, RT and Hallberg, JA 2000, Age relationships in supracrustal sequences of the northen part of the Murchison Terrane, Archaean Yilgarn Craton, Western Australia: a combined field and zircon U–Pb study: Australian Journal of Earth Sciences, v. 47, p. 153–165.

Pidgeon, RT and Wilde, SA 1990, The distribution of 3.0 Ga and 2.7 Ga volcanic episodes in the Yilgarn Craton of Western Australia: Precambrian Research, v. 48, p. 309–325.

Qiu, YM and Groves, DI 1999, Late Archean collision and delamination in the southwestern Yilgarn Craton: the driving force for Archean orogenic lode gold mineralization?: Economic Geology, v. 94, p. 115–122.

Qiu, YM, McNaughton, NJ, Groves, DI and Dalstra, HJ 1999, Ages of internal granitoids in the Southern Cross region, Yilgarn Craton, Western Australia, and their crustal evolution and tectonic implications: Australian Journal of Earth Sciences, v. 46, no. 6, p. 971–981.

Reading, AM, Kennett, BLN and Dentith, MC 2003, Seismic structure of the Yilgarn Craton, Western Australia: Australian Journal of Earth Sciences, v. 50, p. 427–438.

Reading, AM, Kennett, BLN and Goleby, B 2007, New constraints on the seismic structure of West Australia: evidence for terrane stabilization prior to assembly of an ancient continent: Geology, v. 35, p. 379–382.

Rodi, W and Mackie, RL 2001, Nonlinear conjugate gradients algorithm for 2-D magnetotelluric inversion: Geophysics, v. 66, p. 174–187.

Romano, SS, Doublier, MP, Mole, DR, Thebaud, N, Wingate, MTD and Kirkland, CL 2010, Age constraints in the southern part of the Southern Cross Domain of the Yilgarn Craton, *in* Fifth International Archean Symposium Abstracts *edited by* IM Tyler and CM Knox-Robinson: Geological Survey of Western Australia, Record 2010/18, p. 206–208.

Romano, SS, Thebaud, N, Mole, DR, Wingate, MTD, Kirkland, CL in prep., Age implications for Barberton-type komatiites in the Yilgarn Craton, Australian Journal of Earth Sciences.

Savage, MD, Barley, ME and McNaughton, NJ 1996, SHRIMP U–Pb dating of 2.95 to 3.0 Ga intermediate to silicic rocks in the southern Yellowdine Terrane, Yilgarn Craton, *in* Abstracts: Geological Society of Australia; 13th Australian Geological Convention, Canberra, Australian Capital Territory, 1 February 1996, p. 41.

Schiøtte, L and Campbell, IH 1996, Chronology of the Mount Magnet granite–greenstone terrain, Yilgarn Craton, Western Australia: implications for field based predictions of the relative timing of granitoid emplacement: Precambrian Research, v. 78, p. 237–260.

Simpson, F and Bahr, K 2005, Practical magnetotellurics: Cambridge University Press, Cambridge, England, 270p.

Sofoulis, J 1966, Widgiemooltha, WA Sheet SH 51-14: Geological Survey of Western Australia, 1:250 000 Geological Series Explanatory Notes, 25p.

Spratt, JE, Jones, AG, Jackson, VA, Collins, L and Avdeeva, A 2009, Lithospheric geometry of the Wopmay Orogen from a Slave craton to Bear Province magnetotelluric transect: Journal of Geophysical Research, v. 114, no. B01101, doi:10.1029/2007JB005326.

Swager, CP, Goleby, BR, Drummond, BJ, Rattenbury, MS and Williams, PR 1997, Crustal structure of granite–greenstone terranes in the Eastern Goldfields, Yilgarn Craton, as revealed by seismic reflection profiling: Precambrian Research, v. 83, p. 43–56.

Ten Grotenhius, SM, Drury, MR, Peach, CJ and Spiers, CJ 2004, Electrical properties of fine grained olivine: Evidence for grain boundary transport: Journal of Geophysical Research, v. 109, no. B06203, doi:10.1029/2003JB002799.

Thebaud, N, Fiorentini, ML, McCuaig, TC, Miller, J, Barnes, SJ, Joly, A and Doublier, MP 2009, Tectonostratigraphic controls on the localization of Achaean komatiite-hosted nickel–sulphide deposits and camps in the Yilgarn Craton, *in* Challenges to Our Volatile Planet: Goldschmidt Conference 2009, Davos, Switzerland, 20 June 2009; Abstract, p. A1323.

Thebaud, N and Miller, J 2009, U–Pb age constrain on the siliciclastic sediments from the upper supracrustal cover in the Southern Cross greenstone belt, Youanmi Terrane, Western Australia, *in* Smart science for exploration and mining *edited by* PJ Williams: Society for Geology Applied to Mineral Deposits; 10th Biennial SGA Meeting, Townsville, Queensland, 17 August 2009, p. 960–962.

Van Kranendonk, MJ and Ivanic, TJ 2009, A new lithostratigraphic scheme for the northeastern Murchison Domain, Yilgarn Craton, *in* Geological Survey of Western Australia Annual Review 2007–08: Geological Survey of Western Australia, Perth, Western Australia, p. 34–53.

Wang, Q, Campbell, IH and Schiøtte, L 1996, Geochronological constraints on the age of komatiites and nickel mineralisation in the Lake Johnston greenstone belt, Yilgarn Craton, Western Australia: Australian Journal of Earth Sciences, v. 43, p. 381–385.

Wang, Q, Schiøtte, L and Campbell, IH 1998, Geochronology of supracrustal rocks from the Golden Grove area, Murchison Province, Yilgarn Craton, Western Australia: Australian Journal of Earth Sciences, v. 45, no. 4, p. 571–577.

Wight, DE and Bostick, FX 1981, Cascade decimation — a technique for real time estimation of power spectra, *in* Proceedings: Institute of Electrical and Electronic Engineers; International Conference on Acoustics, Speech, and Signal Processing, Atlanta, Georgia, USA, 30 March 1981, p. 626–629.

Wilde, SA 2001, Jimperding and Chittering metamorphic belts, Western Australia — a field guide: Geological Survey of Western Australia, Record 2001/12, 24p.

Wilde, SA, Middleton, MF and Evans, BJ 1996, Terrane accretion in the southwestern Yilgarn Craton: evidence from a deep seismic crustal profile: Precambrian Research, v. 78, p. 179–196.

Wingate, MTD 2007, Proterozoic mafic dykes in the Yilgarn Craton, *in* Proceedings of Kalgoorlie 2007 Conference *edited by* FP Bierlein and CM Knox-Robinson: Geoscience Australia; Kalgoorlie, Western Australia, 25 September 2007; Record 2007/14, p. 80–83.

Wingate, MTD and Kirkland, CL 2010, Compilation of geochronology information, 2010 update: Geological Survey of Western Australia, digital data product.

Witt, WK 1997, Geology of the Ravensthorpe and Cocanarup 1:100 000 sheets: Geological Survey of Western Australia, 1:100 000 Geological Series Explanatory Notes, 26p.

Wu, X, Ferguson, IJ and Jones, AG 2002, Magnetotelluric response and geoelectric structure of the Great Slave Lake shear zone: Earth and Planetary Science Letters, v. 196, p. 35–50.

Wyche, S, Nelson, CS and Riganti, A 2004, 4350–3130 Ma detrital zircons in the Southern Cross Granite–Greenstone Terrane, Western Australia: implications for the early evolution of the Yilgarn Craton: Australian Journal of Earth Sciences, v. 51, p. 31–45.

Yeats, CJ, McNaughton, NJ and Groves, DI 1996, SHRIMP U–Pb geochronological constraints on Archean volcanic-hosted massive sulfide and lode gold mineralization at Mount Gibson, Yilgarn Craton, Western Australia: Economic Geology, v. 91, p. 1354–1371.

Appendix

Apparent resistivity and phase data

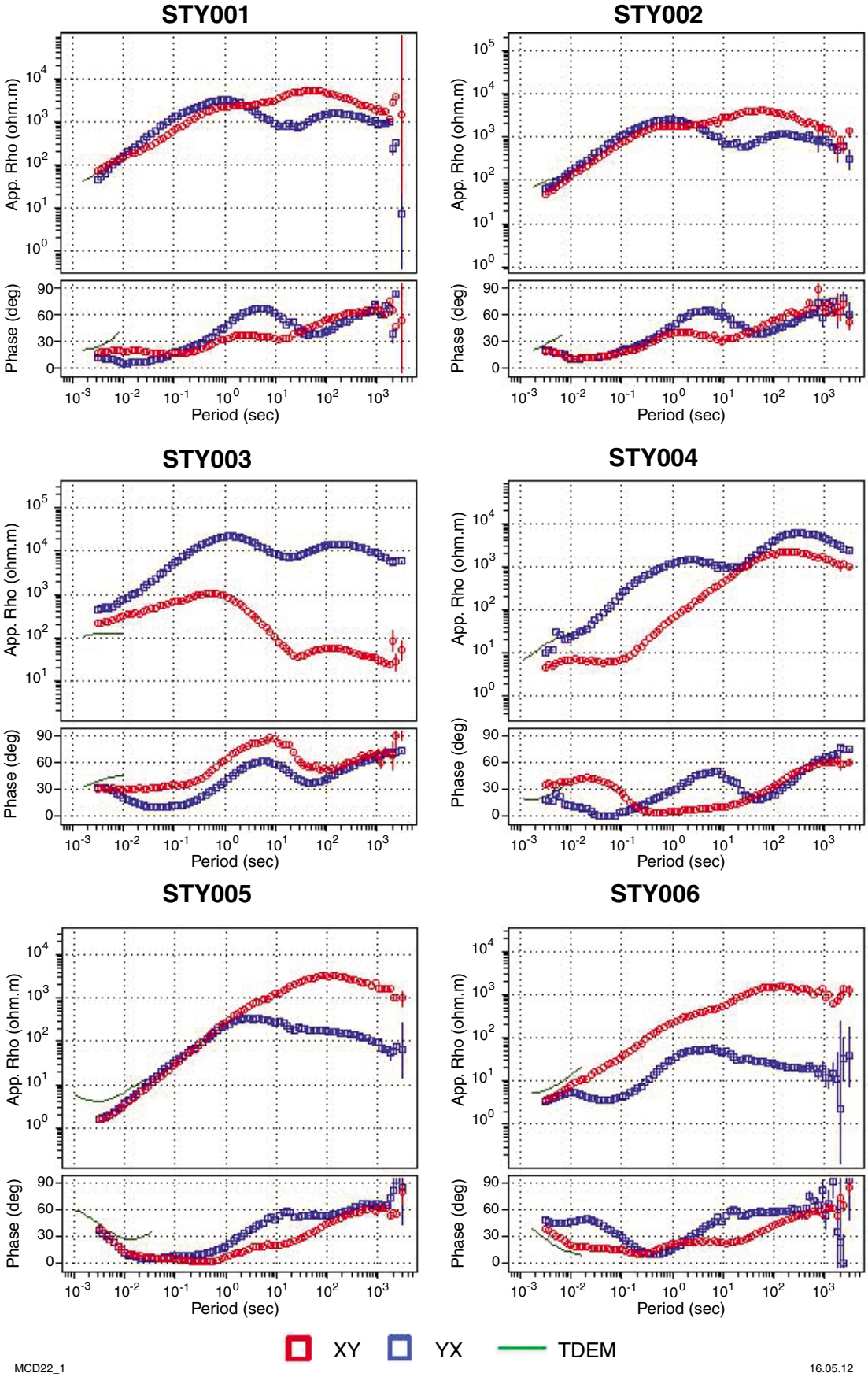

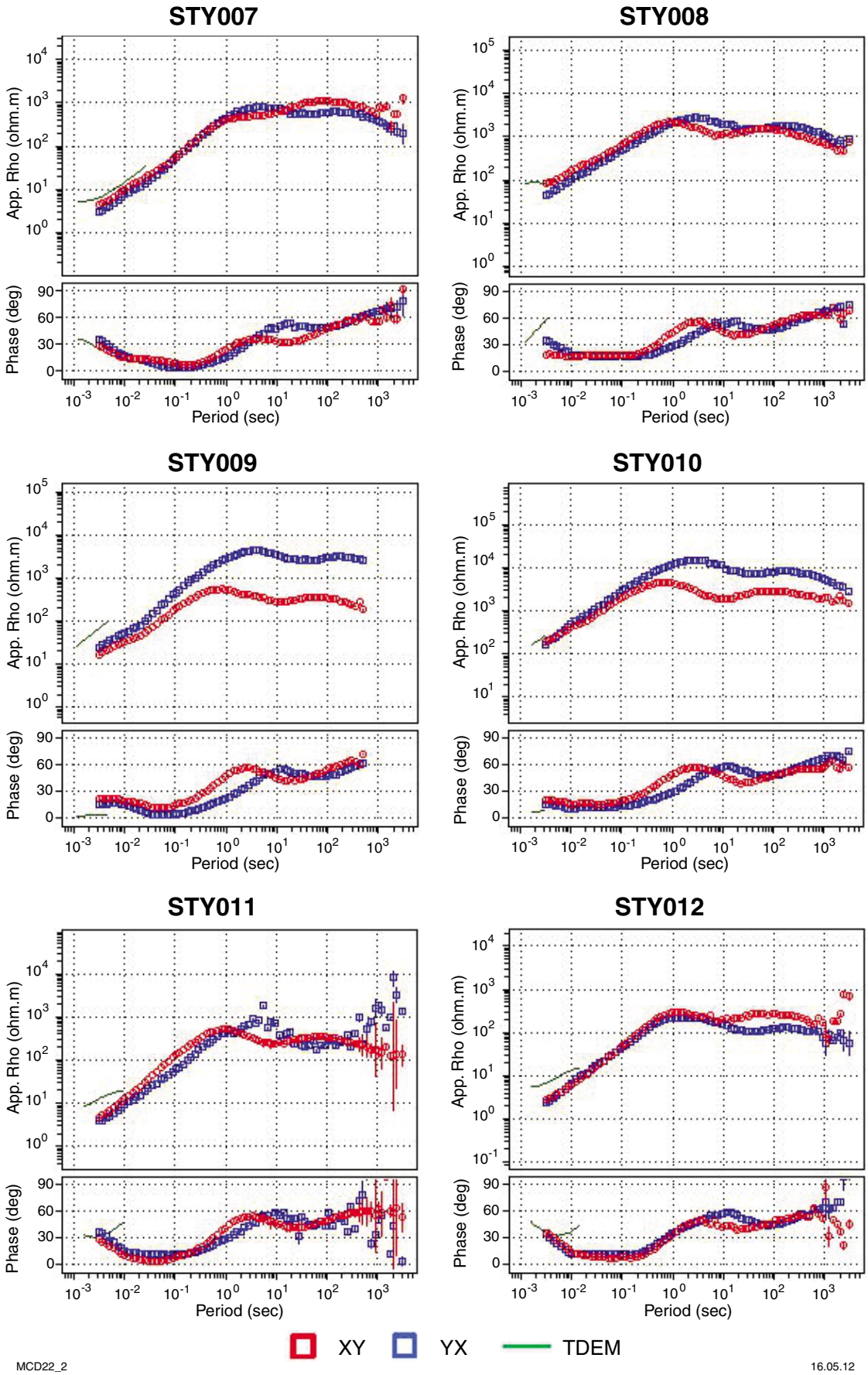
STY007
STY008
STY009
STY010
STY011
STY012
App. Rho (ohm.m)
Phase (deg)
Period (sec)
XY
YX
TDEM
MCD22_2
16.05.12

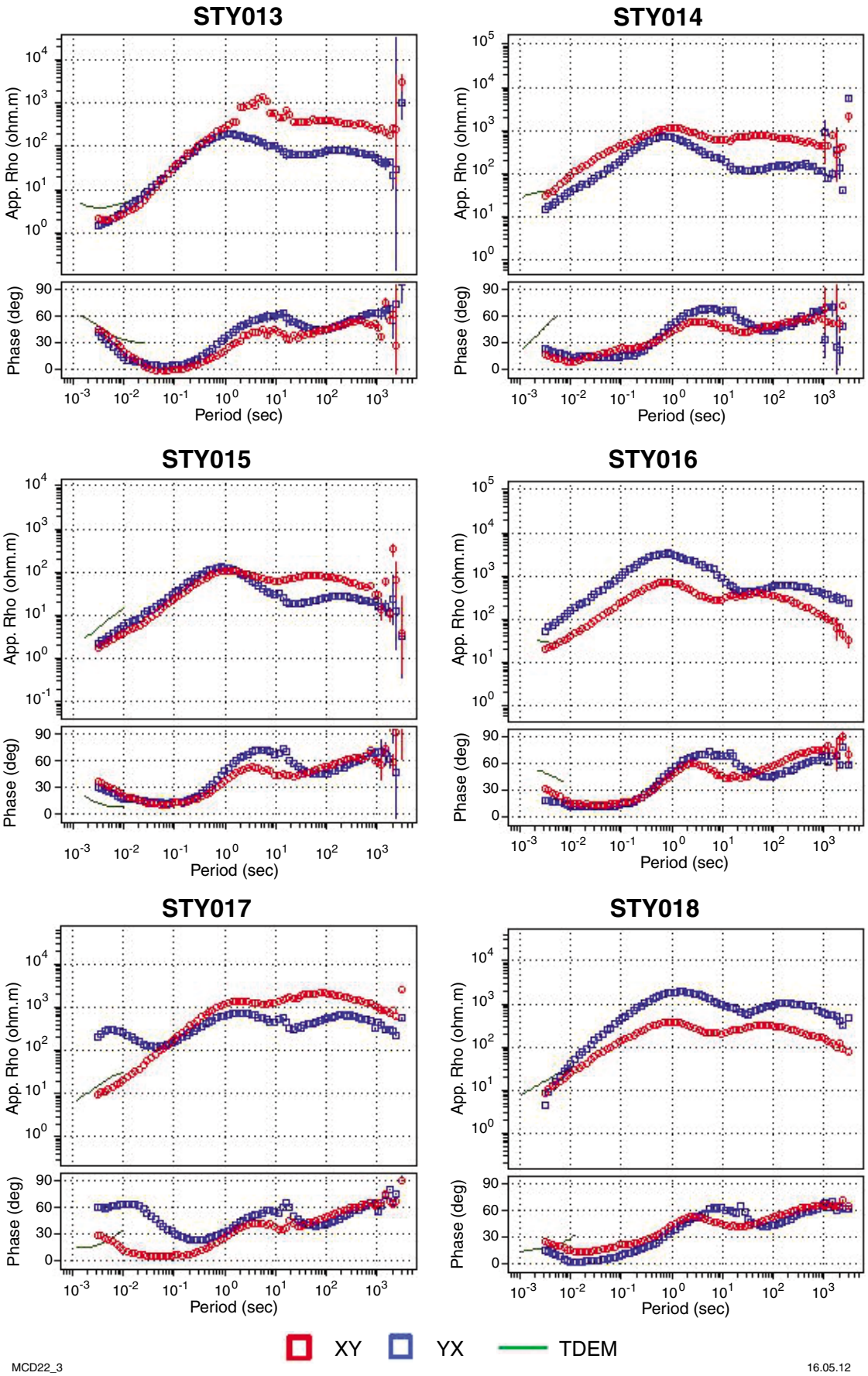
STY013
STY014
STY015
STY016
STY017
STY018
App. Rho (ohm.m)
Phase (deg)
Period (sec)
XY
YX
TDEM
MCD22_3
16.05.12

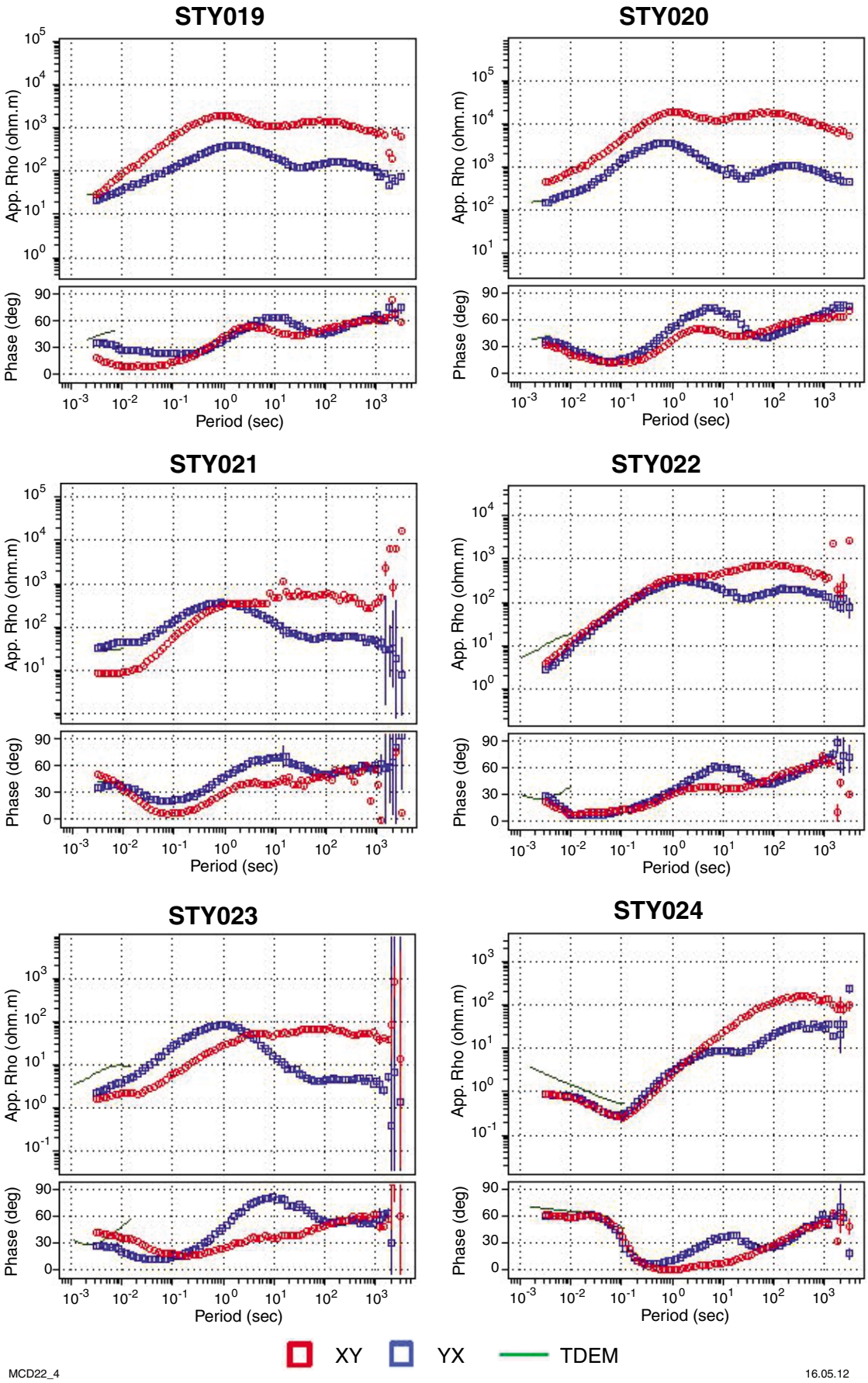
STY019
STY020
STY021
STY022
STY023
STY024
App. Rho (ohm.m)
Phase (deg)
Period (sec)
XY
YX
TDEM
MCD22_4
16.05.12

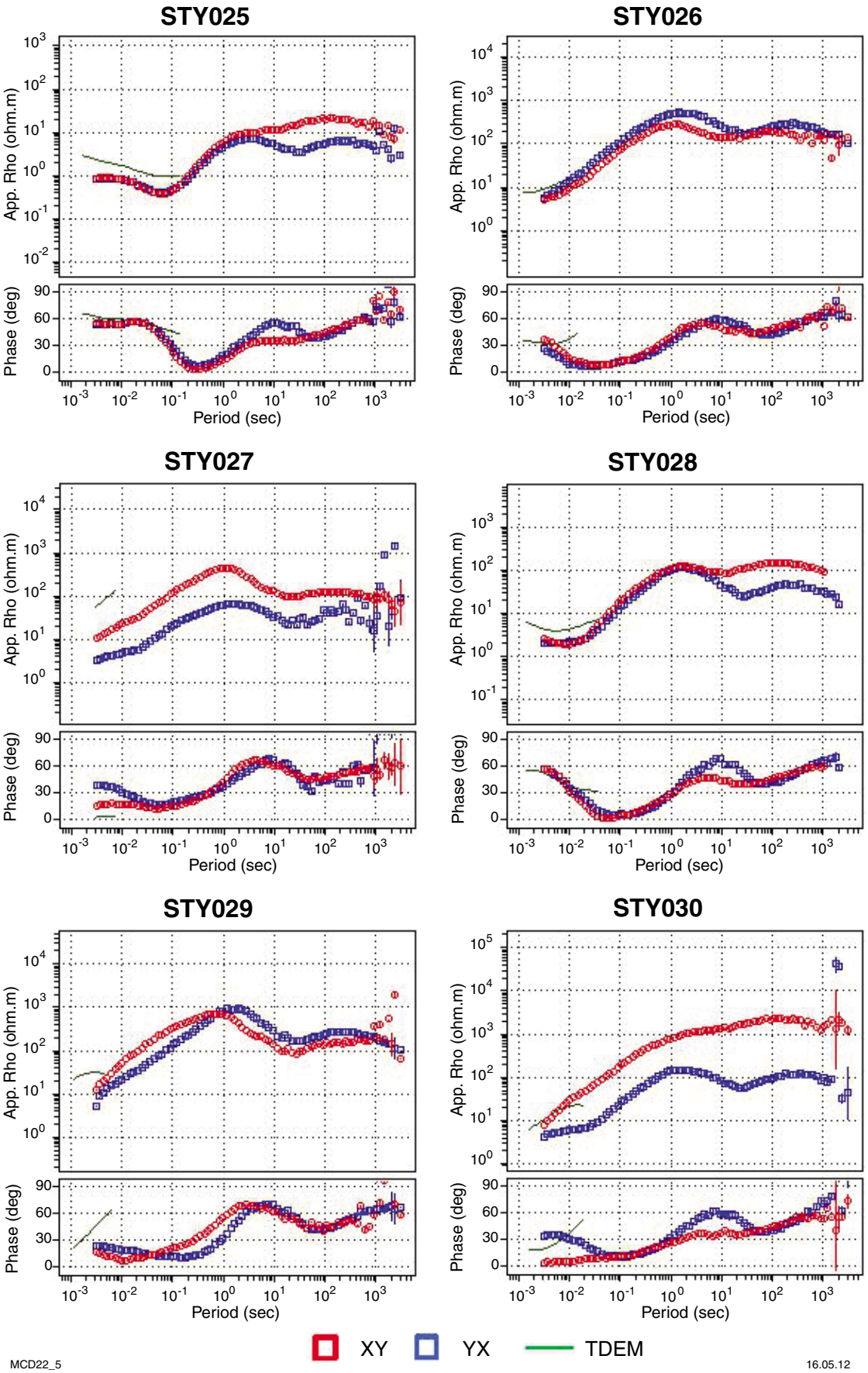
STY025
STY026
STY027
STY028
STY029
STY030
App. Rho (ohm.m)
Phase (deg)
Period (sec)
XY
YX
TDEM
MCD22_5
16.05.12

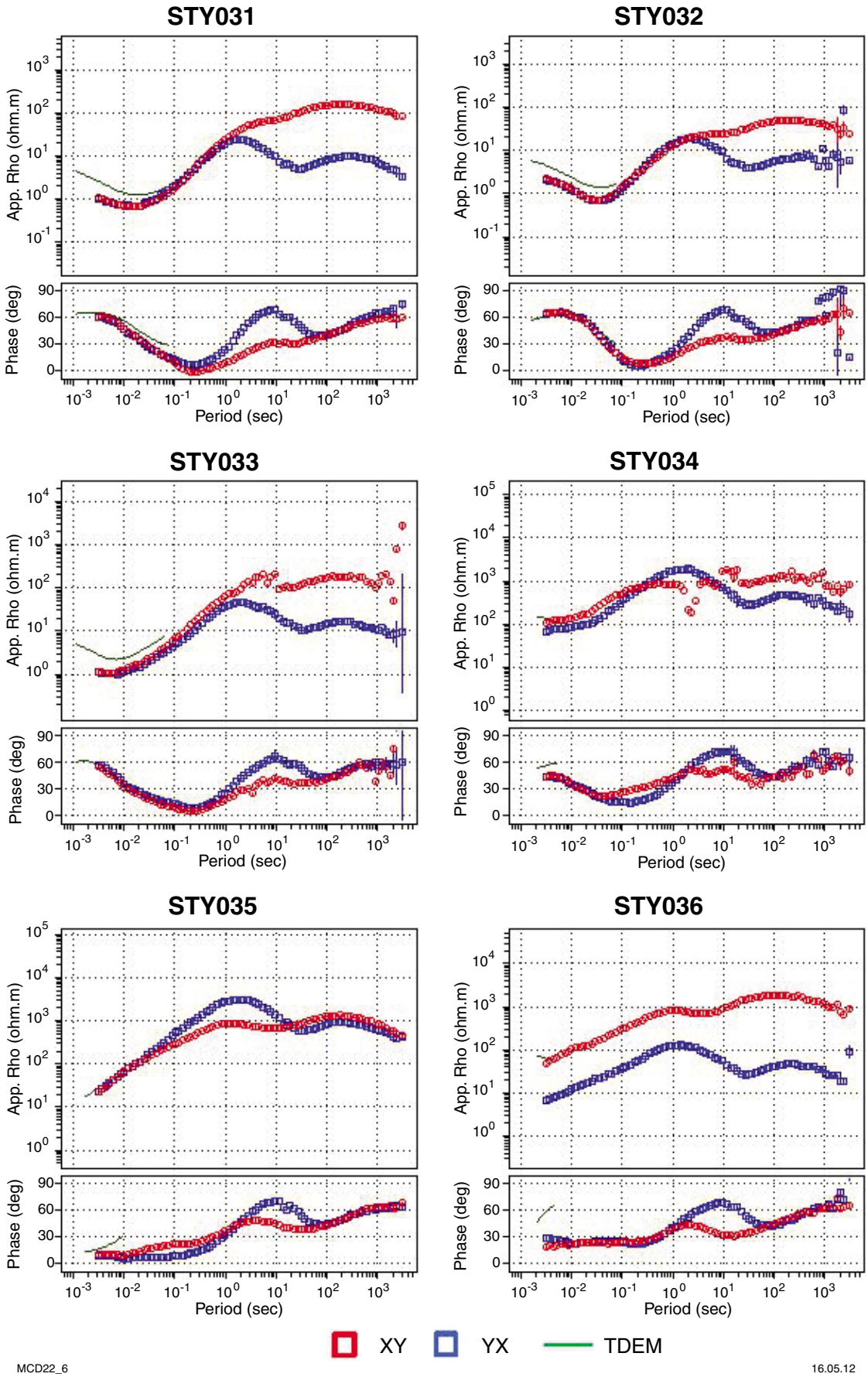
STY031
STY032
STY033
STY034
STY035
STY036
App. Rho (ohm.m)
Phase (deg)
Period (sec)
XY
YX
TDEM
MCD22_6
16.05.12

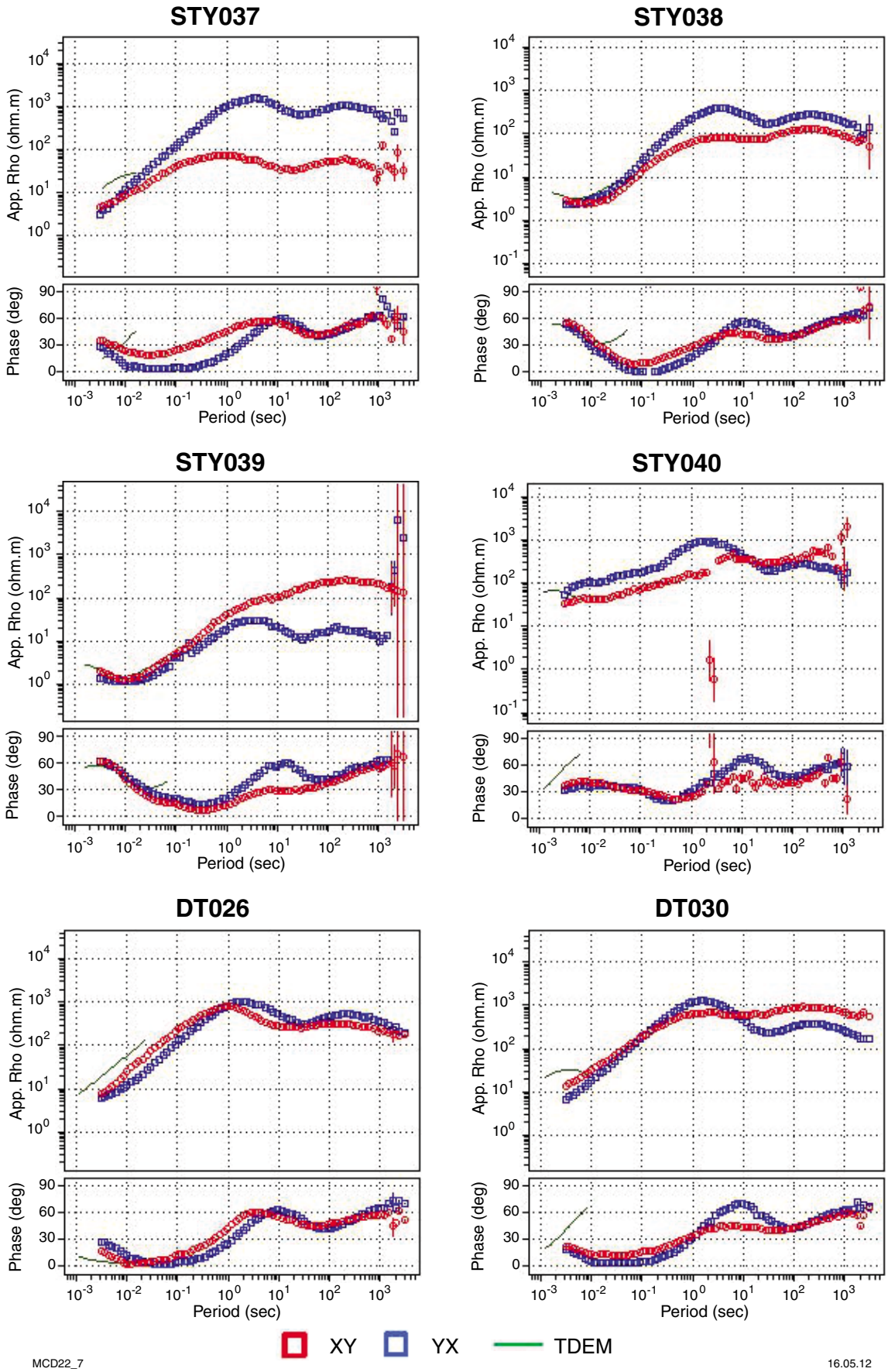
STY037
STY038
STY039
STY040
DT026
DT030
App. Rho (ohm.m)
Phase (deg)
Period (sec)
XY
YX
TDEM
MCD22_7
16.05.12

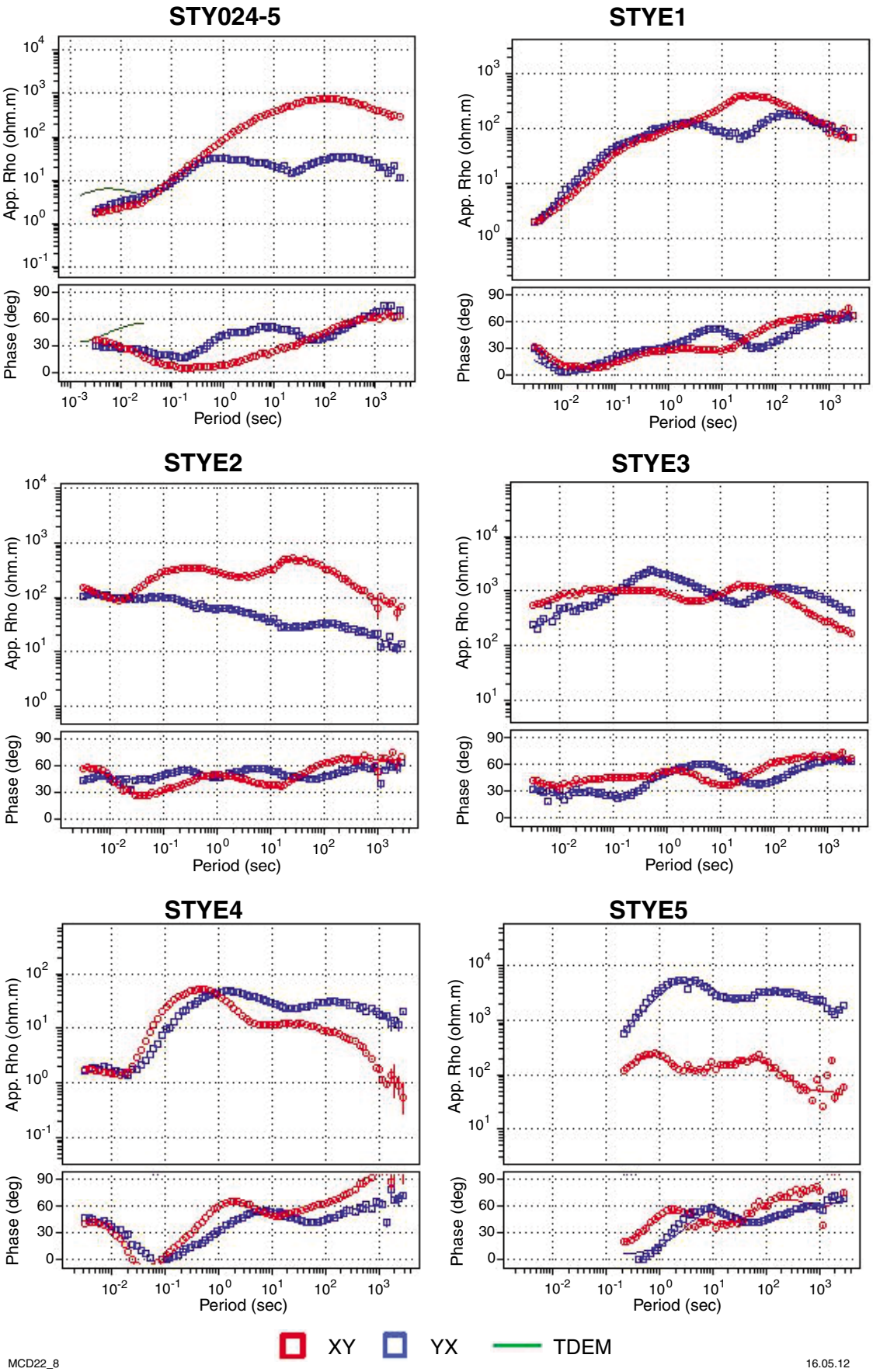
STY024-5
STYE1
STYE2
STYE3
STYE4
STYE5
App. Rho (ohm.m)
Phase (deg)
Period (sec)
XY
YX
TDEM
MCD22_8
16.05.12

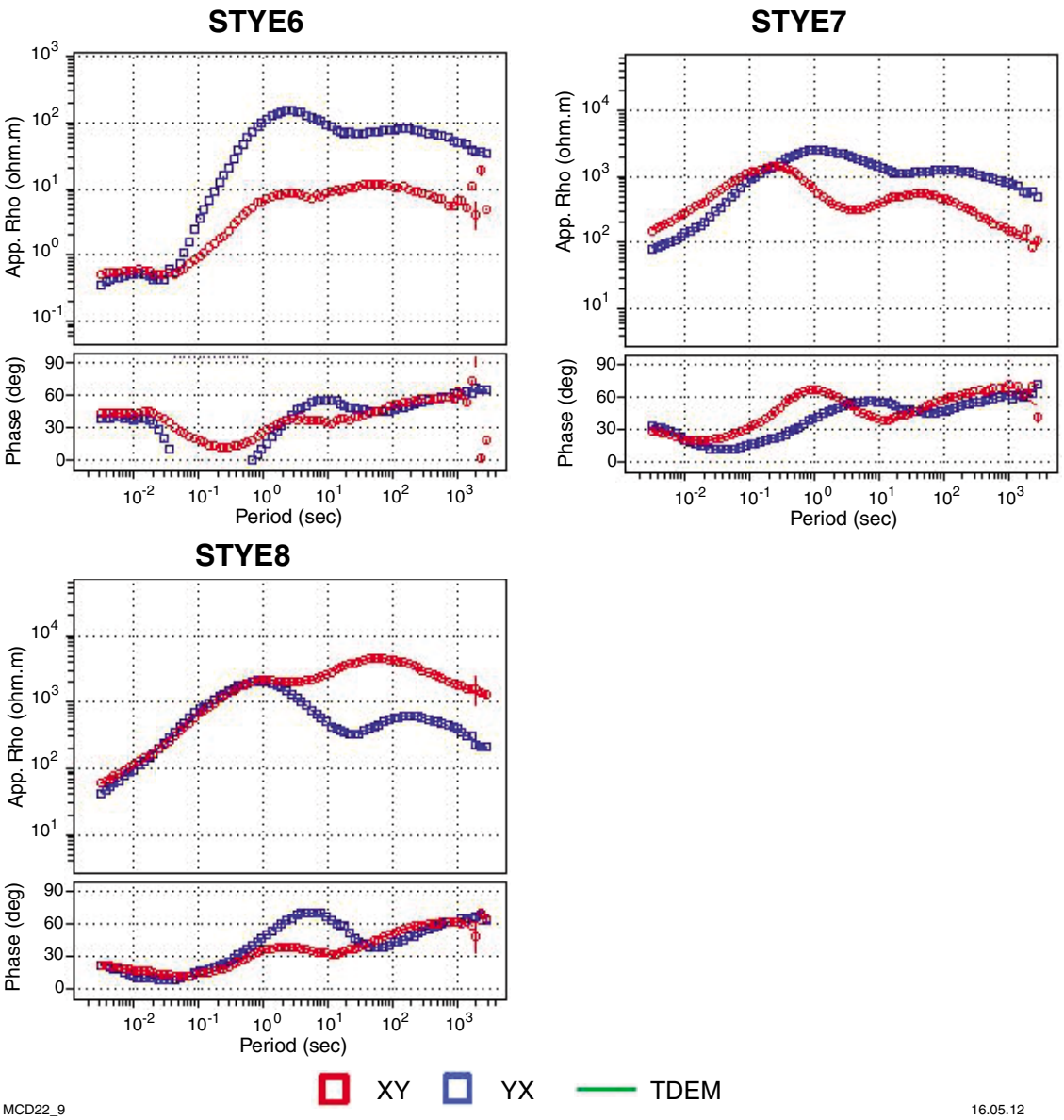
STYE6
STYE7
STYE8
App. Rho (ohm.m)
Phase (deg)
Period (sec)
XY
YX
TDEM
MCD22_9
16.05.12

A 300-km-long magnetotelluric survey, comprising 56 stations, has been completed in the southern Yilgarn Craton over three campaigns during 2009–11. The survey was conducted along an east–west traverse extending from the South West Terrane, across the Southern Cross Domain (Youanmi Terrane), and on to the Kalgoorlie Terrane (Eastern Goldfields Superterrane).

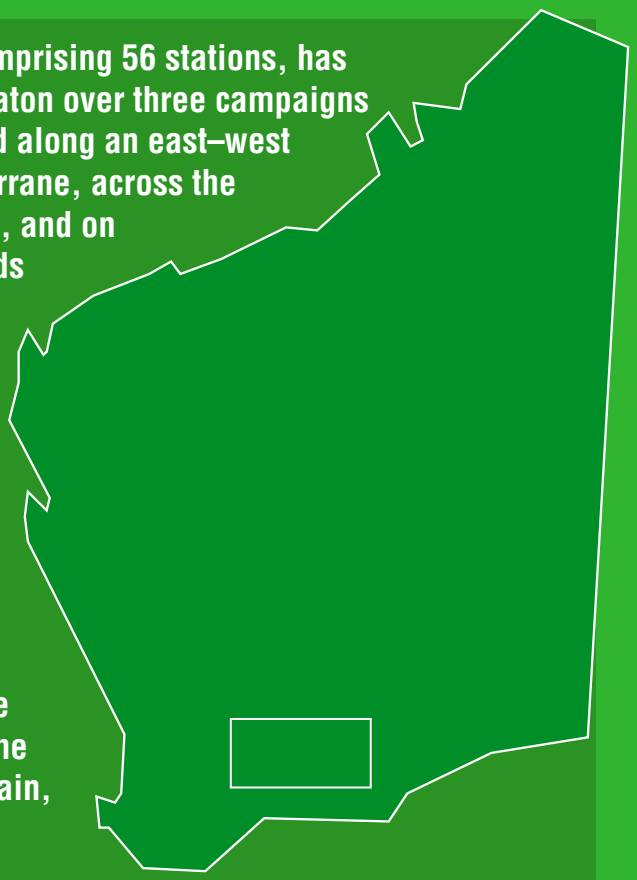

A three-fold subdivision of the local lithosphere is recognized consistent with the geologically and geochemically defined terranes and domains in this part of the Yilgarn Craton. The central unit, interpreted as equivalent to the Southern Cross Domain, has a resistive crust overlying a more conductive mantle. The unit to the east comprises a conductive lower crust overlying a resistive mantle. The eastern margin of the Southern Cross Domain, as inferred from deep crustal and mantle resistivity, lies about 50 km to the west of the Ida Fault mapped at the surface. The western unit has a resistive crust overlying a resistive mantle and is correlated with the South West Terrane.

The magnetotelluric method is demonstrated to be a viable means of mapping the deep-crustal and mantle structure of the Yilgarn Craton.

Further details of geological products and maps produced by the Geological Survey of Western Australia are available from:

Information Centre
Department of Mines and Petroleum
100 Plain Street
EAST PERTH WA 6004
Phone: (08) 9222 3459 Fax: (08) 9222 3444

www.dmp.wa.gov.au/GSWApublications